

Cortex-Grounded Diffusion Models for Brain Image Generation

Fabian Bongratz^{a,b*}, Yitong Li^{a,b*}, Sama Elbaroudy^a,
and Christian Wachinger^{a,b}

^aLab for AI in Medical Imaging, Technical University of Munich, Germany

^bMunich Center for Machine Learning, Germany

*Equal contribution & correspondence: {fabio.bongratz, yi-tong.li}@tum.de

Abstract

Synthetic neuroimaging data can mitigate critical limitations of real-world datasets, including the scarcity of rare phenotypes, domain shifts across scanners, and insufficient longitudinal coverage. However, existing generative models largely rely on weak conditioning signals, such as labels or text, which lack anatomical grounding and often produce biologically implausible outputs. To this end, we introduce *Cor2Vox*, a cortex-grounded generative framework for brain magnetic resonance image (MRI) synthesis that ties image generation to continuous structural priors of the cerebral cortex. It leverages high-resolution cortical surfaces to guide a 3D shape-to-image Brownian bridge diffusion process, enabling topologically faithful synthesis and precise control over underlying anatomies. To support the generation of new, realistic brain shapes, we developed a large-scale statistical shape model of cortical morphology derived from over 33,000 UK Biobank scans. We validated the fidelity of Cor2Vox based on traditional image quality metrics, advanced cortical surface reconstruction, and whole-brain segmentation quality, outperforming many baseline methods. Across three applications, namely (i) anatomically consistent synthesis, (ii) simulation of progressive gray matter atrophy, and (iii) harmonization of in-house frontotemporal dementia scans with public datasets, Cor2Vox preserved fine-grained cortical morphology at the sub-voxel level, exhibiting remarkable robustness to variations in cortical geometry and disease phenotype without retraining.

1 Introduction

Synthetic data can overcome the persistent limitations of real-world medical datasets, such as the limited availability of rare phenotypes, the heterogeneity of imaging devices that introduces domain shifts, and the scarcity of longitudinal data required for disease progression modeling [1]. Despite these advantages, current approaches to medical image generation predominantly rely on implicitly learned associations between low-dimensional labels or short text and high-dimensional image observations [2, 3, 4, 5, 6, 7]. This paradigm lacks explicit control over generated content, making it susceptible to undesired bias [8], memorization of sensitive training data [9], model collapse [10], and implausible hallucinations [11]. In neuroimaging, these challenges are amplified by the complexity of the cerebral cortex, which is inherently difficult to model due to its intricate folds and grooves. Structural inaccuracies and hallucinations often go unnoticed in conventional 2D visualizations and image-based metrics (see Figure 1).

Visual grounding [12] and spatial conditioning [13] have recently gained importance in computer vision by anchoring image generation to a structured, controllable signal as a potential solution to these challenges [12, 13]. Initial work in medical imaging has explored controllable generation by conditioning on segmentation masks [14, 15]. However, such approaches are not directly transferable to neuroimaging. In particular, voxel-level masks generated, for example, by a variational autoencoder (VAE) [16], typically do not guarantee anatomical plausibility and topological correctness. Moreover, brain-related phenotypes, such as those associated with aging or neurodegenerative disorders, manifest as subtle, sub-millimeter morphological changes in the brain structure [17, 18]. Capturing these fine-grained variations requires high-resolution surface meshes rather than coarse voxel masks to ensure faithful representation of neuroanatomy [19, 20].

In this study, we address these issues by introducing *Cor2Vox*, a cortex-grounded generative framework for synthesizing brain magnetic resonance images (MRIs). By explicitly linking image generation to anatomically informed shape constraints of the cerebral cortex, we ensure that outputs remain biologically plausible and reliably reflect the variability observed in the population. The image generation in Cor2Vox is rooted in the Brownian bridge diffusion process, originally proposed for 2D image-to-image translation [21], which is extended to 3D spatially conditioned image synthesis. To enhance anatomical fidelity, we introduce auxiliary shape conditioning based

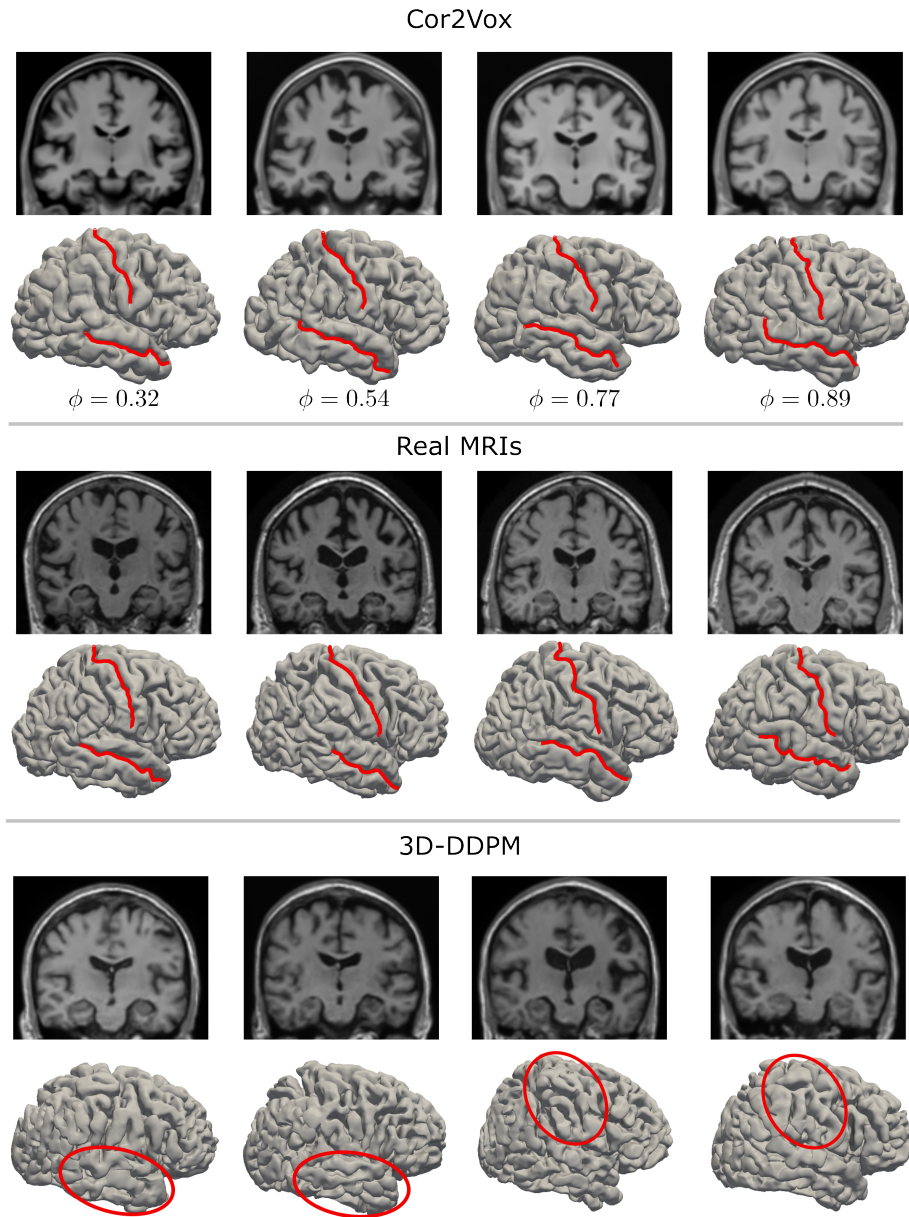


Figure 1: Synthetic MRIs generated by Cor2Vox (top) and 3D-DDPM (bottom), with real MRIs shown for reference (center). Cortical surfaces were reconstructed from the MRIs using Vox2Cortex-Flow. Red lines indicate the central sulcus and superior temporal sulcus, two prominent cortical grooves in human brain anatomy. While Cor2Vox reliably preserves these sulci, they are often absent or significantly distorted in surfaces reconstructed from MRIs generated by 3D-DDPM. Such anatomical irregularities are virtually impossible to detect in conventional 2D slice-based views and require 3D surface reconstructions for reliable assessment. $\phi \in (0, 1)$ denotes the spherical interpolation factor in the Cor2Vox shape model.

on signed distance fields (SDFs) and structural masks during the reverse diffusion process, enabling precise guidance and alignment with cortical geometry. In contrast to conventional denoising diffusion probabilistic models (DDPMs) [22], which are based on unstructured Gaussian priors, the Brownian bridge diffusion in Cor2Vox maps directly from a dedicated cortex SDF to an output image, thereby eliminating the dependence on an unstructured latent space. As part of Cor2Vox, we present a large-scale statistical shape model of the human cerebral cortex, built upon deep learning-based mesh reconstructions of cortical boundaries with over 163,000 vertices per hemisphere. This shape model, derived from over 33,000 UK Biobank brain MRI scans [23], enables the synthesis of unseen, anatomically plausible cortical geometries by navigating the shape space that captures realistic brain anatomy in the population. Importantly, the generative capabilities of Cor2Vox surpass previous methods for simulating neuroanatomical change, which are typically constrained to morphing pre-existing scans [24, 25, 26, 27, 28, 29], limiting their ability to generate unseen anatomies.

Our experiments showcase three practical applications of Cor2Vox. First, we utilize Cor2Vox to synthesize anatomically consistent brain MRIs that adhere to gyral folding patterns and reflect parcellation-based cortical thickness. Second, we conduct mesh-based continuous deformations to simulate progressive cortical atrophy at the sub-voxel level, which is important for studying neurodegenerative trajectories and benchmarking of cortical thickness estimation methods. Finally, we employ Cor2Vox to harmonize MR images across the ADNI database and in-house frontotemporal dementia (FTD) cases. To this end, we leverage Cor2Vox’s ability to disentangle brain morphology, which captures characteristic atrophy patterns in FTD, from its image appearance that is typically affected by scanner hardware and acquisition protocols. Compared to our previous related work [30], we also provide a more extensive evaluation of Cor2Vox’s image fidelity, using traditional image fidelity metrics, advanced cortical surface reconstruction based on Vox2Cortex-Flow [31], and automatic whole-brain segmentation quality assessment based on SynthSeg+ [32]. Code to reproduce our results is available at <https://github.com/ai-med/Cor2Vox>.

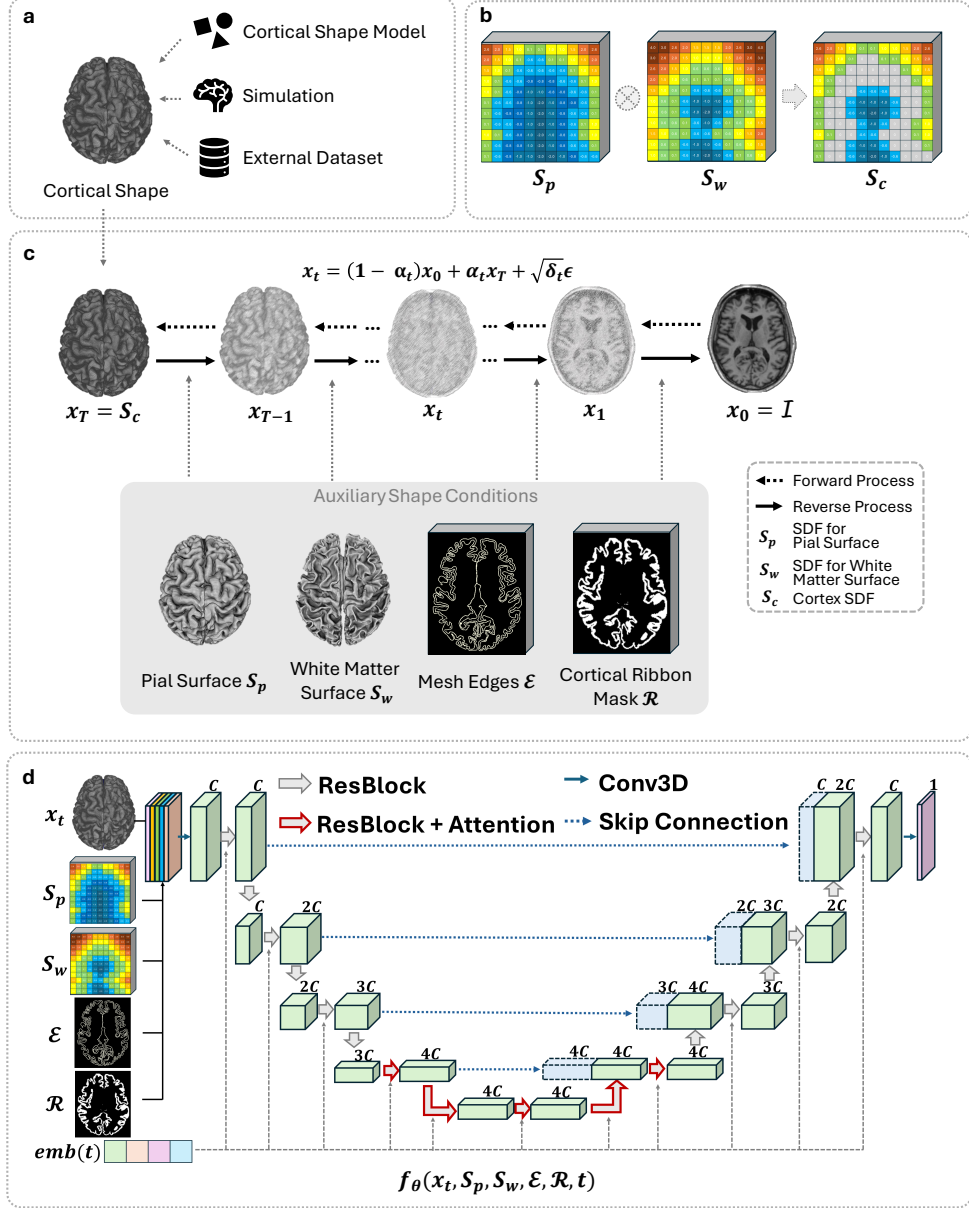


Figure 2: Cor2Vox overview. a, In dependence on the application, input cortical surfaces can be created based on a statistical shape model of the cerebral cortex, surface-based simulations, or existing shapes from external databases. b, The cortical surface meshes, i.e., pial (S_p) and white matter (S_w) surfaces, are converted into a joint cortex signed distance field (SDF), S_c . c, Cor2Vox leverages a shape-to-image Brownian bridge diffusion process to learn a stochastic mapping f_θ from the spatial condition S_c to the output image I . During the reverse diffusion process, auxiliary shape conditions are incorporated to improve geometric consistency with the input condition. d, A residual 3D UNet with convolutional and attention blocks is implemented for the prediction of the reverse diffusion process.

2 Materials and Methods

2.1 Cortex-conditioned brain image generation

2.1.1 Overview of Cor2Vox

An overview of Cor2Vox is presented in Figure 2, illustrating the high-level workflow and model architecture. Conceptually, Cor2Vox synthesizes brain MR images conditioned on cortical surfaces that define the cerebral cortex shape a priori, serving as a spatial constraint for image generation. The first step (Figure 2a) defines the cortical shape, for which we propose three complementary strategies: (i) sampling from a population-based shape model, which allows high-resolution cortices to be generated and their variability to be modeled by traversing the cortical shape manifold in latent space, (ii) applying simulated morphological alterations, such as localized cortical thinning, and (iii) importing cortical surfaces from external datasets, enabling cross-dataset harmonization.

In the second step (Figure 2b), the input cortical shape, represented as 3D surface meshes, is converted into a signed distance field (SDF) representation of the cortex, denoted \mathcal{S}_c . This representation combines SDFs of the inner (white matter) boundary \mathcal{S}_w and outer (pial) boundary \mathcal{S}_p . Based on this spatial condition, Cor2Vox generates an MRI via a Brownian bridge diffusion process (Figure 2c). The forward process analytically maps between the image and the cortical condition, while the reverse diffusion is guided by auxiliary shape constraints, including \mathcal{S}_p , \mathcal{S}_w , a binarized edge map \mathcal{E} , and a cortical ribbon mask \mathcal{R} . Figure 2d illustrates the denoising network architecture, which uses a 3D residual U-Net with convolutional and attention blocks, trained to predict x_{t-1} from x_t during reverse diffusion.

2.1.2 Representing the cortex as a signed distance field

We propose to use an SDF-based representation of the cortex as a starting point for brain image generation, cf. Figure 2. For a closed surface $\mathcal{S} \subset \mathbb{R}^3$, an SDF is defined as

$$g : \Omega \subseteq \mathbb{R}^3 \rightarrow \mathbb{R}, \quad (1)$$

where $g(x)$ denotes the signed orthogonal distance from a point $x \in \Omega$ to the surface \mathcal{S} . The sign convention typically assigns negative values to points inside \mathcal{S} and positive values to points outside; the zero-level set, i.e., $g(x) = 0$,

corresponds to the surface itself. When sampled densely, SDFs align with the grid-like structure of 3D image data, a property that is essential for implementing the Brownian bridge-based diffusion process within our architecture.

However, representing the cortical ribbon with an SDF is not straightforward, as it is bounded by two closely spaced surfaces: the outer pial surface and the inner white matter surface. Each of these surfaces is traditionally provided as a separate mesh for each hemisphere. As a first preprocessing step, we merged the pial and white matter meshes into unified representations, denoted by \mathcal{M}_p and \mathcal{M}_w , respectively. From these meshes, we constructed a unified cortex SDF, \mathcal{S}_c , which serves as the primary source input for our shape-to-image framework. To achieve this, we first converted the pial and white matter meshes into their respective dense SDFs, \mathcal{S}_p and \mathcal{S}_w . Next, we fused the two SDFs into a unified cortical representation, \mathcal{S}_c , following a region-specific logic: i) Region outside the cortex: when both \mathcal{S}_p and \mathcal{S}_w are positive, we assign \mathcal{S}_c the value of \mathcal{S}_p , which is the distance to the pial surface, i.e., the closer surface in this case. ii) Cortex region: when \mathcal{S}_p and \mathcal{S}_w have opposite signs, the point is part of the cortex. Here, we set \mathcal{S}_c to zero, creating a clear delineation of the cortical region. We also extracted this zone as a binary mask, \mathcal{R} . iii) Region enclosed by the cortical ribbon: when both \mathcal{S}_p and \mathcal{S}_w are negative, \mathcal{S}_c takes the value of \mathcal{S}_w , which is the distance to the white matter surface, i.e., the closer surface in this case. The detailed procedure is also illustrated in Figure S5.

Our goal is to synthesize a 3D MRI volume $\mathcal{I} \in \mathbb{R}^{H \times W \times D}$ that faithfully reflects the cortical geometry encoded by the SDF \mathcal{S}_c . Formally, this requires learning a mapping

$$f_\theta : \mathbb{R}^{H \times W \times D} \longrightarrow \mathbb{R}^{H \times W \times D}, \quad (2)$$

such that $\mathcal{I} = f_\theta(\mathcal{S}_c)$ parameterized by θ . Inspired by recent advances in image-to-image translation [21, 33], we model f_θ using a neural network-based Brownian bridge diffusion process within our Cor2Vox framework, as illustrated in Figure 2.

2.1.3 Brownian bridge diffusion process

In standard Denoising Diffusion Probabilistic Models (DDPMs) [22], incorporating spatial conditions is inherently challenging because generation typically begins from pure Gaussian noise, $\varepsilon \sim \mathcal{N}(0, \mathbf{I})$. In contrast, the Brownian Bridge Diffusion Model (BBDM) [21] establishes a direct mapping between structured source and target distributions. In our setting,

Algorithm 1 Training Process of Cor2Vox

```

1: repeat
2:   Paired data  $\mathbf{x}_0 \sim q(\mathcal{I})$ ,  $\mathbf{x}_T \sim q(\mathcal{S}_c)$  and auxiliary conditions  $\mathcal{C} = (\mathcal{S}_p, \mathcal{S}_w, \mathcal{E}, \mathcal{R}) \sim q(\mathcal{S}_p, \mathcal{S}_w, \mathcal{E}, \mathcal{R})$ 
3:   Timestep  $t \sim \text{Uniform}(1, \dots, T)$ 
4:   Gaussian noise  $\varepsilon \sim \mathcal{N}(0, \mathbf{I})$ 
5:   Forward diffusion  $\mathbf{x}_t = (1 - \alpha_t)\mathbf{x}_0 + \alpha_t\mathbf{x}_T + \sqrt{\delta_t}\varepsilon$ 
6:   Take gradient descent step on  $\nabla_{\theta} \|\alpha_t(\mathbf{x}_T - \mathbf{x}_0) + \sqrt{\delta_t}\varepsilon - f_{\theta}(\mathbf{x}_t, \mathcal{C}, t)\|_1$ 
7: until converged

```

the Brownian bridge connects the cortex SDF \mathcal{S}_c to its corresponding MRI volume \mathcal{I} , enabling a direct, anatomically informed conditioning in the diffusion process. This formulation allows training directly on paired samples $(\mathbf{x}_T, \mathbf{x}_0) \sim q_{\text{data}}(\mathcal{S}_c, \mathcal{I})$, thereby eliminating the need for Gaussian noise as an initial state.

Forward diffusion process. Beginning with an initial state \mathbf{x}_0 (MRI volume \mathcal{I}), the forward process progressively transforms it to the destination state \mathbf{x}_T (shape prior \mathcal{S}_c) over a series of stochastic timesteps. This process is defined as follows:

$$q(\mathbf{x}_t \mid \mathbf{x}_0, \mathbf{x}_T) = \mathcal{N}(\mathbf{x}_t; (1 - \alpha_t)\mathbf{x}_0 + \alpha_t\mathbf{x}_T, \delta_t\mathbf{I}), \quad \mathbf{x}_T \equiv \mathcal{S}_c, \quad (3)$$

where $\alpha_t = t/T$, T is the total number of steps in the diffusion process, and $\delta_t = 2(\alpha_t - \alpha_t^2)$ is the variance term. In analogy to [21], the transition probability between two consecutive steps in the Brownian bridge is given as:

$$\begin{aligned} q_{\text{BB}}(\mathbf{x}_t \mid \mathbf{x}_{t-1}, \mathbf{x}_T) &= \mathcal{N}\left(\mathbf{x}_t; \frac{1 - \alpha_t}{1 - \alpha_{t-1}}\mathbf{x}_{t-1} + \left(\alpha_t - \frac{1 - \alpha_t}{1 - \alpha_{t-1}}\alpha_{t-1}\right)\mathbf{x}_T, \delta_{t|t-1}\mathbf{I}\right), \\ \delta_{t|t-1} &= \delta_t - \delta_{t-1} \frac{(1 - \alpha_t)^2}{(1 - \alpha_{t-1})^2}. \end{aligned} \quad (4)$$

The variance term δ_t follows a bridge-like schedule. At the start of the diffusion process ($t = 0$), it is set to zero, $\delta_0 = 0$, ensuring the process begins from the MRI image, i.e., $\mathbf{x}_0 \equiv \mathcal{I}$. As diffusion progresses, δ_t gradually increases, reaching its maximum value $\delta_{\text{max}} = \delta_{T/2} = 1/2$ at the midpoint, introducing the highest level of stochasticity during the transition between image and

Algorithm 2 Sampling Process of Cor2Vox

```
1: Sample conditional input  $x_T = \mathcal{S}_c \sim q(\mathcal{S}_c)$ ,  $\mathcal{C} = (\mathcal{S}_p, \mathcal{S}_w, \mathcal{E}, \mathcal{R}) \sim q(\mathcal{S}_p, \mathcal{S}_w, \mathcal{E}, \mathcal{R})$ 
2: for  $t = T, \dots, 1$  do
3:   if  $t > 1$  then  $\varepsilon \sim \mathcal{N}(0, \mathbf{I})$ , else  $\varepsilon = 0$ 
4:    $x_{t-1} = c_{xt}\mathbf{x}_t + c_{st}\mathcal{S}_c - c_{ft}f_\theta(\mathbf{x}_t, \mathcal{C}, t) + \sqrt{\tilde{\delta}_t}\varepsilon$ 
5: end for
6: return  $x_0$ 
```

shape. Beyond this point, the variance decreases symmetrically, returning to zero at the final timestep ($t = T$), where $\alpha_T = 1$, guaranteeing convergence to the target SDF \mathcal{S}_c . This schedule enables a smooth yet stochastic transformation from the image domain \mathcal{I} to the shape domain \mathcal{S}_c , effectively learning a continuous path between two fixed states and establishing a direct link between anatomical shape and its visual representation.

Reverse diffusion process. The reverse Brownian bridge process begins directly at the input condition $\mathbf{x}_T \equiv \mathcal{S}_c$ and ends at the MRI (\mathcal{I}), essentially reversing the forward process by predicting \mathbf{x}_{t-1} from \mathbf{x}_t . However, we propose to incorporate additional structural representations of the cortex as auxiliary inputs to the denoising model. Specifically, these auxiliary representations include i) the pial surface SDF \mathcal{S}_p , ii) the white matter surface SDF \mathcal{S}_w , iii) a binary edge map \mathcal{E} capturing pial and white matter boundaries, and iv) the cortical ribbon mask \mathcal{R} , cf. Section 2.1.2. These conditions are jointly represented as $\mathcal{C} = (\mathcal{S}_p, \mathcal{S}_w, \mathcal{E}, \mathcal{R})$ and provided to the model at each timestep t of the reverse process, which we found to improve the geometric consistency considerably, cf. Section 3.5.

Considering the additional guidance by the auxiliary conditions, the transition probability in our reverse process is given as:

$$p_\theta(\mathbf{x}_{t-1} \mid \mathbf{x}_t, \mathcal{C}, \mathcal{S}_c) = \mathcal{N}(\mathbf{x}_{t-1}; \boldsymbol{\mu}_\theta(\mathbf{x}_t, \mathcal{C}, t), \tilde{\delta}_t \mathbf{I}), \quad (5)$$

where $\boldsymbol{\mu}_\theta(\mathbf{x}_t, \mathcal{C}, t)$ represents the predicted mean value and $\tilde{\delta}_t$ denotes the noise variance at each timestep. In our implementation, we follow the reparameterization strategy used in DDPM [22], which trains a neural network $f_\theta(\cdot)$ to predict solely the noise rather than the mean $\boldsymbol{\mu}_\theta$. Precisely, we re-

formulate μ_θ as a linear combination of \mathbf{x}_t , \mathcal{S}_c , and the estimated part f_θ :

$$\begin{aligned}\mu_\theta(\mathbf{x}_t, \mathcal{C}, \mathcal{S}_c, t) &= c_{xt}\mathbf{x}_t + c_{st}\mathcal{S}_c + c_{ft}f_\theta(\mathbf{x}_t, \mathcal{C}, t), \text{ where} \\ c_{xt} &= \frac{\delta_{t-1}}{\delta_t} \frac{1 - \alpha_t}{1 - \alpha_{t-1}} + \frac{\delta_{t|t-1}}{\delta_t} (1 - \alpha_{t-1}), \\ c_{st} &= \alpha_{t-1} - \alpha_t \frac{1 - \alpha_t}{1 - \alpha_{t-1}} \frac{\delta_{t-1}}{\delta_t}, \text{ and} \\ c_{ft} &= (1 - \alpha_{t-1}) \frac{\delta_{t|t-1}}{\delta_t}.\end{aligned}\quad (6)$$

The parameters c_{xt} , c_{st} , and c_{ft} are non-trainable since they are derived from α_t , α_{t-1} , θ_t , and θ_{t-1} . The variance term $\tilde{\delta}_t$ does not need to be learned either; it can be derived analytically as $\tilde{\delta}_t = \frac{\delta_{t|t-1}\delta_{t-1}}{\delta_t}$.

Training. The training process is designed to minimize the disparity between the joint distribution predicted by f_θ and the training data. This is accomplished by optimizing the Evidence Lower Bound (ELBO), which provides a lower bound on the log-likelihood of the data and is defined as follows:

$$\begin{aligned}\text{ELBO} &= -\mathbb{E}_q(\text{D}_{\text{KL}}(q_{\text{BB}}(\mathbf{x}_T | \mathbf{x}_0, \mathcal{S}_c) \| p(\mathbf{x}_T | \mathcal{C}, \mathcal{S}_c))) \\ &\quad + \sum_{t=2}^T \text{D}_{\text{KL}}(q_{\text{BB}}(\mathbf{x}_{t-1} | \mathbf{x}_t, \mathbf{x}_0, \mathcal{S}_c) \| p_\theta(\mathbf{x}_{t-1} | \mathbf{x}_t, \mathcal{C}, \mathcal{S}_c)) \\ &\quad - \log p_\theta(\mathbf{x}_0 | \mathcal{C}, \mathcal{S}_c).\end{aligned}\quad (7)$$

By combining the ELBO with Eq. (4)(5)(6), our loss function is given by:

$$\mathcal{L}_{\text{Cor2Vox}} = \mathbb{E}_{\mathbf{x}_0, \mathcal{S}_c, \varepsilon \sim \mathcal{N}(0, \mathbf{I})} \left[\left\| \alpha_t(\mathcal{S}_c - \mathbf{x}_0) + \sqrt{\delta_t} \varepsilon - f_\theta(\mathbf{x}_t, \mathcal{C}, t) \right\|_1 \right]. \quad (8)$$

By minimizing this loss at each timestep, the model learns to reverse the forward diffusion process, i.e., to generate brain images based on a cortical shape condition. For an algorithmic description of the training process, see Algorithm 1.

Sampling. Based on the reverse diffusion formulation, Cor2Vox generates new images by adhering to the following iteration:

$$\mathbf{x}_{t-1} = c_{xt}\mathbf{x}_t + c_{st}\mathcal{S}_c - c_{ft}f_\theta(\mathbf{x}_t, \mathcal{C}, t) + \sqrt{\tilde{\delta}_t} \varepsilon, \quad (9)$$

where $\varepsilon \sim \mathcal{N}(0, \mathbf{I})$ when $t > 1$, otherwise $\varepsilon = 0$. We accelerate the sampling process by employing the DDIM (Denoising Diffusion Implicit Models) [34] strategy. This approach utilizes a non-Markovian process, enabling faster and more direct sampling while preserving the same marginal distributions as the original Markovian inference. For an algorithmic description of the sampling process, see Algorithm 2.

2.1.4 Model architecture and training parameters

To parameterize f_θ , we utilize a 3D UNet architecture, based on the ADM model [35] and adapted for 3D volumetric data. We set the channel sizes for the four residual stages to [64, 128, 192, 256]. Our model further leverages global attention with 4 heads and 64 channels at a downsampling factor of 8. To integrate the timestep information, we use adaptive group normalization within each residual block. In our experiments, we trained for 400 epochs on a single NVIDIA H100 94GB GPU using the Adam optimizer [36]. We set the initial learning rate to 1×10^{-4} , which is reduced by a factor of 0.5 upon reaching a plateau. We used a batch size of 2, and an exponential moving average (EMA) rate of 0.995. For the diffusion process, we used 1,000 timesteps for training. For inference, we adopt the DDIM sampling strategy [34] with only 10 timesteps, which represents an effective balance between image quality and computational efficiency.

2.1.5 Cortical shape model

To promote anatomical plausibility in generated brain images while capturing realistic population-level variability, we propose to anchor the generative process to an explicit statistical shape model of the cerebral cortex. Samples drawn from this shape model serve directly as inputs to our cortex-to-image module described in Section 2.1, ensuring that generated images remain consistent with biologically informed structural priors. To this end, we developed an approach based on principal component analysis (PCA), which we will describe in the following.

Creating a shape model for the cerebral cortex. PCA-based shape models are well-established for anatomical structures such as bones and organs [37, 38, 39]. However, these structures are commonly represented by comparably small meshes or sets of landmarks, rarely exceeding 10,000

points. In contrast, modeling the cerebral cortex requires over 160,000 vertices per brain hemisphere, as provided by V2C-Flow [31]. Moreover, the ribbon-like structure introduces additional challenges that prevents the direct application of existing shape modeling approaches that were usually designed for single-surface structures.

Starting from pre-registered T1-weighted MRI scans in MNI152 standard space, V2C-Flow produces white matter and pial cortical surfaces with inherent vertex-wise correspondence to the FsAverage template (163,842 vertices) [40]. We compute midthickness surfaces $\mathcal{M}^{\text{mid}} \in \mathbb{R}^{163,842 \times 3}$, not provided by default, by averaging the coordinates of corresponding pial and white matter vertices, while preserving the original mesh connectivity. Additionally, vertex-wise cortical thickness $\mathcal{T} \in \mathbb{R}^{163,842}$ is estimated via bidirectional vertex-to-face distance measurements between the two surfaces. Together, the midthickness geometry and cortical thickness form a compact representation of the cortical ribbon, which integrates seamlessly into a PCA-based shape model. We fit separate PCA models for each hemisphere, retaining 8,192 latent components per side. This configuration explains over 95% of population-level variability in the UKB dataset and achieves an average point-wise mesh reconstruction error (L2) below 1 mm on the held-out validation set.

Traversing the manifold of cortical shapes. To sample new cortical geometries, we propose a spherical interpolation (slerp) [41]-based approach in PCA latent space. Thereby, we ensure that the sampled left and right hemispheres fit together, and we stay on the manifold of realistic brain anatomies. See the provided video in the supplementary material for a visualization of this approach.

First, we embed two randomly chosen cortices, given as tuples $(\mathcal{M}_1^{\text{mid}}, \mathcal{T}_1)$, $(\mathcal{M}_2^{\text{mid}}, \mathcal{T}_2)$, via PCA:

$$\mathbf{e}_1, \mathbf{e}_2 = \text{PCA}((\mathcal{M}_1^{\text{mid}}, \mathcal{T}_1)), \text{PCA}((\mathcal{M}_2^{\text{mid}}, \mathcal{T}_2)); \quad \mathbf{e}_1, \mathbf{e}_2 \in \mathbb{R}^{8192}. \quad (10)$$

Based on the normalized embeddings $\hat{\mathbf{e}}_1 = \frac{\mathbf{e}_1}{\|\mathbf{e}_1\|}$, $\hat{\mathbf{e}}_2 = \frac{\mathbf{e}_2}{\|\mathbf{e}_2\|}$, an arbitrarily chosen interpolation factor $\phi \in (0, 1)$, angle $\beta = \arccos(\hat{\mathbf{e}}_1^T \hat{\mathbf{e}}_2)$, and radius $r = \|\mathbf{e}_1\|$, we obtain a new embedding

$$\mathbf{e}_\phi = r \text{slerp}(\mathbf{e}_1, \mathbf{e}_2) = r \left(\frac{\sin((1 - \phi)\beta)}{\sin(\beta)} \mathbf{e}_1 + \frac{\sin(\phi\beta)}{\sin(\beta)} \mathbf{e}_2 \right), \quad (11)$$

and, finally, the corresponding cortex representation from the inverse PCA:

$$(\mathcal{M}_\phi^{\text{mid}}, \mathcal{T}_\phi) = \text{PCA}^{-1}(\mathbf{e}_\phi). \quad (12)$$

Compared to a standard linear interpolation, the spherical interpolation avoids the bias toward the population mean, which would result in overly smooth and therefore implausible cortical surfaces (see Figure S3).

2.2 Simulating cortical atrophy

Simulating cortical atrophy, i.e., the progressive thinning and loss of cortical tissue over time, in MRIs is challenging since the longitudinal alterations in the cerebral cortex typically lie considerably below the image resolution of 1 mm [42, 43, 44]. Yet, the surface-based approach and the deliberate combination of white matter and pial surfaces in Cor2Vox enable fine-grained continuous simulations. Specifically, we deform pial surfaces towards white matter surfaces by moving pial vertices iteratively in the direction of surface normals. The deformed surfaces can be used directly as input for the cortex-to-image module in Cor2Vox.

2.3 Implementation of baseline methods

For best comparison to Cor2Vox, we implemented the baseline methods used to benchmark the performance of our model in a consistent manner. Specifically, we extended Pix2Pix [45] and BBDM [21], which were originally developed for 2D images, to 3D volumetric data. For BBDM, we further applied its diffusion process directly in image space instead of a latent space, which aligns with the implementation of Med-DDPM [46] and Cor2Vox. Med-DDPM [46] is a dedicated 3D diffusion model for brain MRI generation based on conditional segmentation masks. In our implementation of Med-DDPM, we switched from slice-wise to volumetric intensity scaling and changed the denoising target from noise to the denoised image, which considerably enhanced its performance. For all baseline models, we trained two versions, based on the mesh edge maps (\mathcal{E}) and cortical ribbon masks (\mathcal{R}). These representations closely resemble the conditions employed in their original works. In addition, to isolate the effect of the Brownian bridge process, we developed a variant of our model, namely Cor2Vox/DDPM. In this variant, we replaced the Brownian bridge process with a standard denoising diffusion process, while

keeping all other components, including the auxiliary shape conditions. This allows us to directly compare the efficacy of the two diffusion processes for our application.

2.4 Evaluation metrics

To thoroughly evaluate the performance of our model, we assessed the quality of the generated MRIs using a combination of traditional image fidelity metrics, cortical surface-based geometric consistency, and automated image quality assessment.

Image fidelity. In our evaluation, we used two standard metrics for traditional image comparisons, Peak Signal-to-Noise Ratio (PSNR) and Structural Similarity Index Measure (SSIM). For unpaired data, where a direct ground-truth comparison is not possible (relevant only for experiments in Section 3.4), we computed a Multi-Reference SSIM (MR-SSIM) score. This score is calculated by averaging the SSIM between a generated image and ten randomly selected images from the reference dataset.

Surface accuracy. To evaluate the consistency of generated MRIs with the cortex condition, we use deep learning-based cortical surface reconstruction with V2C-Flow [31]. Specifically, we compute the Average Symmetric Surface Distance (ASSD) between the input surfaces \mathcal{S} and surfaces extracted by V2C-Flow from the synthetic images $\hat{\mathcal{S}}$:

$$\text{ASSD}(\hat{\mathcal{S}}, \mathcal{S}) = \frac{\sum_{p \in \hat{\mathcal{P}}} d(p, \mathcal{S}) + \sum_{p \in \mathcal{P}} d(p, \hat{\mathcal{S}})}{|\hat{\mathcal{P}}| + |\mathcal{P}|}, \quad (13)$$

where $\hat{\mathcal{P}} \subset \hat{\mathcal{S}}$ and $\mathcal{P} \subset S$ are 100,000 surface points, respectively. The point-face distance $d(p, \mathcal{M})$ measures the orthogonal distance from a point $p \in \mathbb{R}^3$ to its closest point on the surface mesh \mathcal{M} (lower is better).

Automatic image quality assessment. To validate the practical utility of our generated MRIs, we also assess their quality for downstream image processing. We use the automatic quality control built into the SynthSeg+ framework [47], which calculates the quality of cortical and subcortical segmentations derived from the generated brain images in the form of an estimated Dice coefficient between 0 and 1 (higher is better).

2.5 Computational software and hardware

Our software is based on Python (v3.10.14) and PyTorch (v2.1.0). During the preparation of the manuscript, we used several other Python libraries to support data analysis, including pandas (v2.2.1), scipy (v1.10.0), torchvision (v0.16.0), scikit-learn (v1.0.2), nibabel (v5.2.1), monai (v1.3.0), torchio (v0.19.6), pytorch3d (v0.6.1), and trimesh (v4.6.5). Image processing and training of V2C-Flow involved FreeSurfer (v7.2). Training Cor2Vox on a single NVIDIA H100 GPU on a shared computing cluster had an average runtime of 2.16 seconds per iteration, whereas the synthesis during inference took around a minute per instance. For fitting the PCA-based shape model, we used a high-performance computing infrastructure with 2TB of main memory, which took approximately two days per PCA.

2.6 Data and preprocessing

In this study, we used data from the Alzheimer’s Disease Neuroimaging Initiative (ADNI) [48]. Specifically, we used T1-weighted brain magnetic resonance images (MRIs) from cognitively normal subjects, subjects diagnosed with mild cognitive impairment (MCI), and Alzheimer’s disease (AD). All scans were registered to MNI152 standard space via affine registration using NiftyReg (v1.5.69). Cortical surfaces were then extracted with a pre-trained Vox2Cortex-Flow (V2C-Flow) [31] model, using identical train/validation/test splits, comprising 1,155/169/323 samples, respectively. We used only baseline scans from ADNI to avoid subject bias.

For the cortical shape model, we used data from the UK Biobank (UKB) Imaging Study [49]. Initially, we used 1,000 scans for fine-tuning the V2C-Flow model based on previously extracted FreeSurfer [19] surfaces. The remaining scans were then processed with this fine-tuned V2C-Flow model, resulting in 38,432 white matter and pial surfaces for each brain hemisphere. After excluding outliers based on an initially fitted PCA model and a per-component threshold of 1,000 and keeping 10% of samples for validation, 33,403 UKB scans remained for fitting our cortical PCA model.

Lastly, we used 10 in-house clinical scans obtained by Klinikum Rechts der Isar (TUM Klinikum, Munich, Germany). These scans are from 10 subjects diagnosed with behavioral-variant frontotemporal dementia (bvFTD). The diagnosis was established using clinical criteria, FDG-PET metabolism information, and cerebrospinal fluid biomarkers.

We created signed distance fields (SDFs) for the white matter and pial surfaces from the V2C-Flow meshes using a KDTree [50] implemented in Scipy (v1.10.0). Both brain hemispheres were combined. Internally, all models use an internal resolution of 128^3 voxels. For evaluation, we rescaled all outputs back to MNI space, 1 mm isotropic resolution. For the computation of PSNR and SSIM metrics, we used SynthStrip [51] to skull-strip both the generated images and the original images (`orig.mgz` files from FreeSurfer) to prevent scanner noise in the background of the original scans from confounding the evaluation. Despite this, all models were trained to produce the entire MRI, including the skull and background, which is reflected in our visualizations.

3 Results

3.1 Image fidelity comparison to baseline methods

Figure 3 reports the image fidelity of Cor2Vox in comparison to previous related baseline methods based on our ADNI test set (see also Table S1). Specifically, we assessed the methods’ abilities to preserve visual quality across the whole brain and maintain fine-grained geometric consistency with the cortical input conditions. We computed traditional quantitative metrics, including the structural similarity index measure (SSIM) and peak signal-to-noise ratio (PSNR), between the synthesized and ground-truth MRIs. Additionally, we reconstructed white matter (WM) and pial cortical surfaces from the synthetic MRIs using Vox2Cortex-Flow, which enabled sub-voxel evaluation of surface fidelity.

WM surfaces in Cor2Vox were, on average, 0.04 mm more accurate than those from the second-best method, a 3D-extended version of the Brownian bridge diffusion model (BBDM) [21], as measured by the average symmetric surface distance (ASSD, Figure 3b). This represents an approximate 10% improvement in surface accuracy, which was consistently observed across the entire cortex (see Figure 3a). Similarly, the average reconstruction error in pial surfaces was 0.03 mm lower in Cor2Vox compared to the BBDM. The improvements for both the WM and pial surfaces in terms of ASSD were significant, as indicated by a paired Wilcoxon signed-rank test ($p < 10^{-7}$). A variant of our model, Cor2Vox/DDPM, which employs a DDPM-like diffusion process, outperformed Med-DDPM [46], a dedicated model for spa-

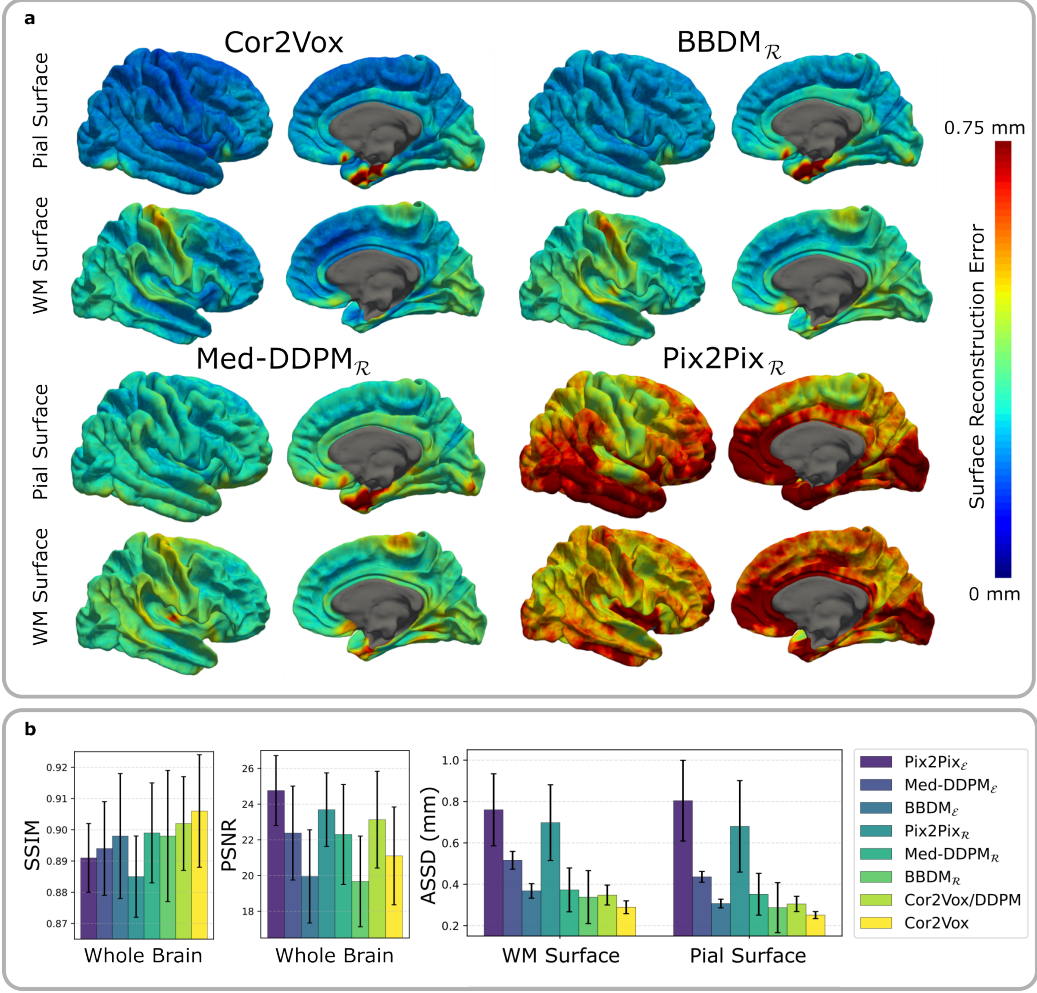


Figure 3: Image fidelity comparison of implemented methods for 3D brain MRI synthesis based on conditional cortical surfaces from the ADNI test set ($n = 323$). Pix2Pix and BBDM were adapted for 3D generation. \mathcal{R} and \mathcal{E} indicate cortical ribbon mask and edge map inputs, respectively. a, Average vertex-wise reconstruction errors between input conditions and white matter (WM) and pial cortical surfaces reconstructed from the synthetic MRIs (lower is better). Visualizations are based on the FsAverage template. b, Structural similarity index measure (SSIM \uparrow) and peak signal-to-noise ratio (PSNR \uparrow) for whole-brain image fidelity and average symmetric surface distance (ASSD \downarrow , mm) for geometric consistency of right hemisphere WM and pial cortical surfaces (see Table S1 for left hemisphere values). Bar plots show the mean and standard deviation (error bar) across all samples in the test set.

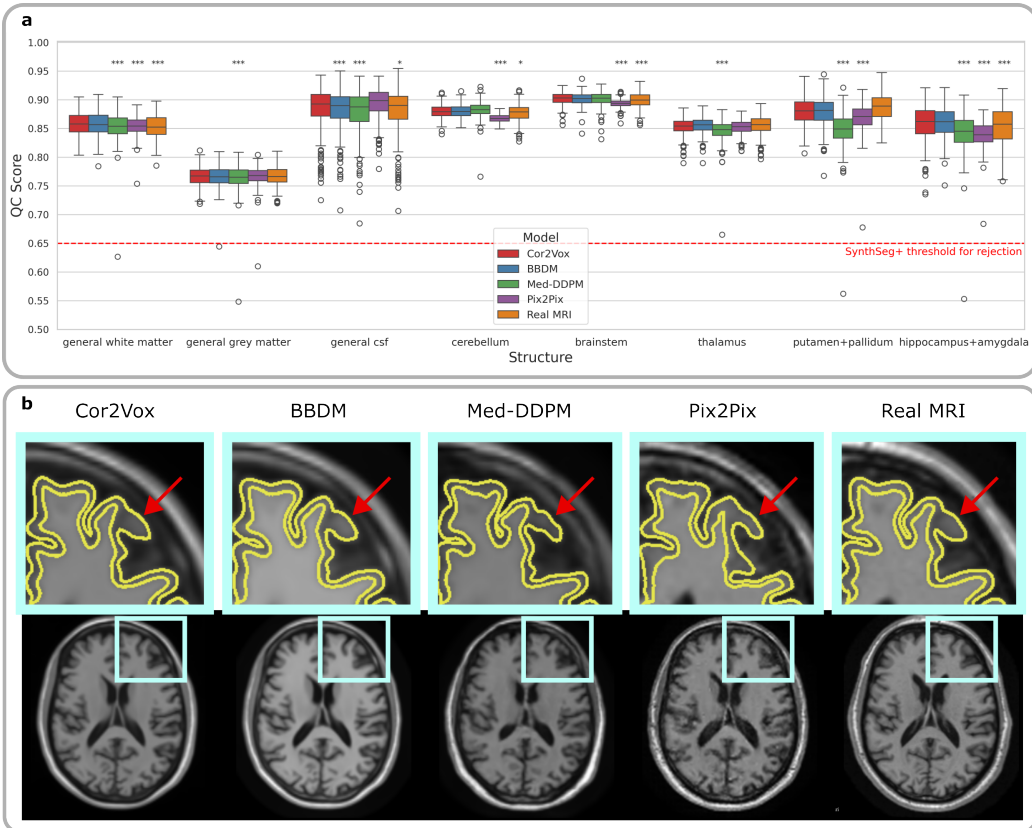


Figure 4: Brain segmentation quality and qualitative synthesis results. a, SynthSeg+-based automatic quality control (QC) scores of segmented brain structures in the synthetic MRIs. Asterisks indicate significant improvement of Cor2Vox over other methods as determined by a Wilcoxon signed rank test and Benjamini-Hochberg correction; ***: $p < 0.001$, **: $p < 0.01$, *: $p < 0.05$. The horizontal red line indicates the recommended quality threshold for downstream processing of 0.65 [47]. b, Synthetic MRIs from different methods and the real counterpart, visualized together with reconstructed cortical contours. All MRIs broadly show the same cortical geometry, with differences marked by red arrows.

tially conditioned brain MRI generation, even after deliberate optimization of this method; see Section 2.3 for implementation details. Yet, DDPM-based models could not keep up with the best Brownian bridge diffusion-based approaches (Cor2Vox and BBDM). Moreover, a 3D-extended version of Pix2Pix [45], which leverages generative adversarial networks (GANs) [52], was not competitive with the diffusion-based models in terms of geometric consistency. Overall, cortical ribbon masks (\mathcal{R}) consistently outperformed binarized edge maps (\mathcal{E}) as input conditions in our experiments, both of which are commonly used representations for spatial constraints in the original works presenting Pix2Pix, Med-DDPM, and BBDM.

In terms of traditional whole-brain image fidelity metrics (Figure 3b), Cor2Vox achieved the highest SSIM scores across all methods, while Pix2Pix yielded the best PSNR performance. However, prior studies have highlighted limitations of these conventional image metrics in the context of brain MRI synthesis [53, 54], and have advocated for segmentation-based evaluation using SynthSeg [32, 47]. Accordingly, we adopted SynthSeg+ [47] for a more task-relevant assessment of image quality. The results, presented in Figure 4a, demonstrate the superiority of Cor2Vox across many brain structures, with every individual sample surpassing the recommended quality threshold of 0.65 across all segmented brain structures. Finally, qualitative inspection of the synthesized MRIs, visualized in Figure 4b, further shows the high cortical fidelity of Cor2Vox, with the reconstructed contours closely matching those of the original scan.

3.2 Anatomically consistent brain generation

While generative models can generate new brain images by sampling from abstract latent spaces, ensuring biological plausibility requires a population-based shape model. However, capturing cortical variability across individuals remains a major challenge due to the cortex’s intricate folding patterns, regional heterogeneity, and substantial inter-subject anatomical differences. To date, no comprehensive model of this variability exists. Leveraging cortical surface meshes from over 33,000 UK Biobank brain MRI scans, we constructed a detailed statistical model of cortical anatomy (see Section 2.1.5 for details). By traversing the latent space of this model via spherical interpolation, we ensure that sampled shapes lie on the manifold of anatomically realistic cortical geometry (cf. Figure S3).

The sequence of cortical surfaces in Figure 5a illustrates this process,

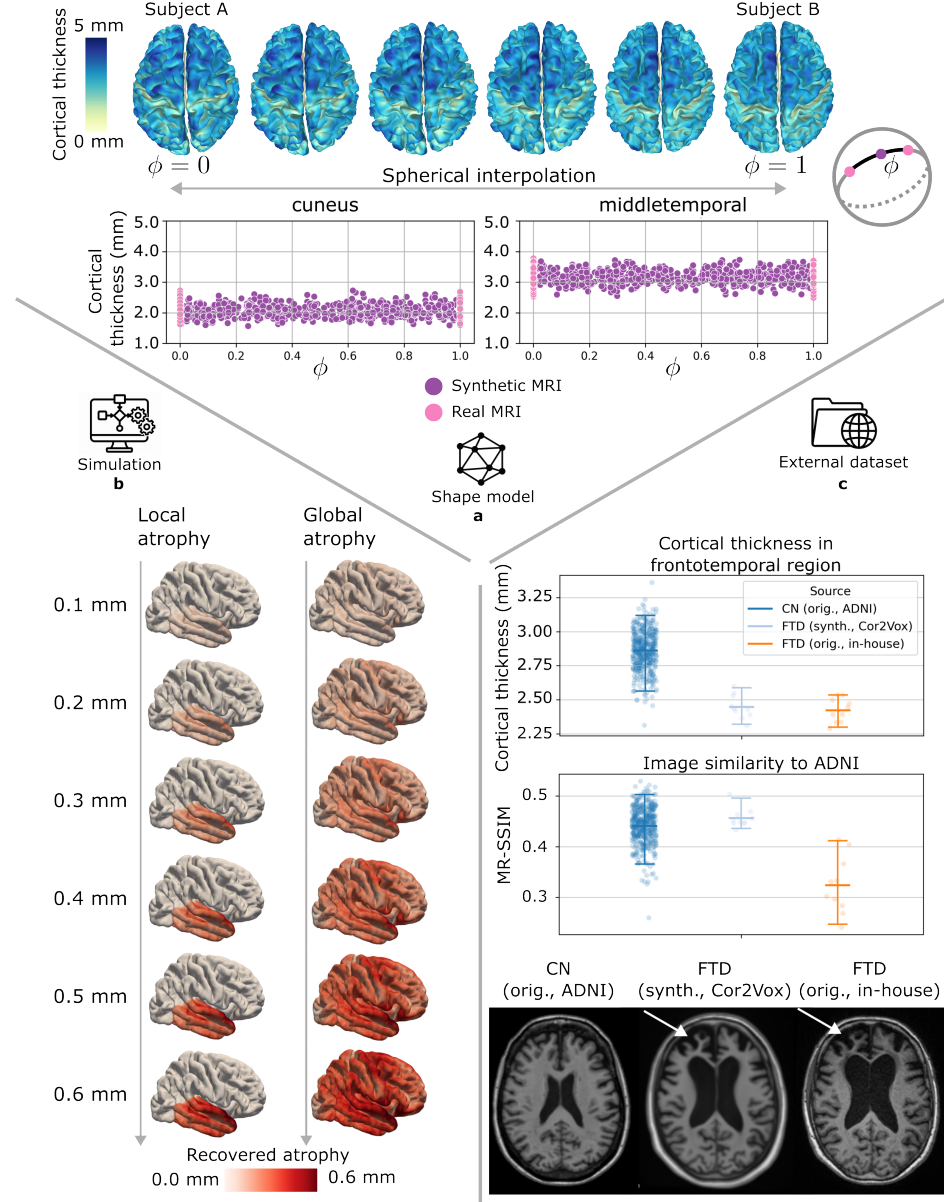


Figure 5: Results from three real-world applications of Cor2Vox. a, Surface plots visualize the anatomically consistent sampling of cortices by spherical interpolation in shape space for an arbitrary pair of UKB subjects. Scatter plots show cortical thickness in the cuneus and middle temporal regions of synthetic and real data based on randomly sampled subject pairs. b, Simulation of progressive cortical atrophy; surface plots show average recovered atrophy from 124 synthetic MRIs (1 mm isotropic resolution), in dependence on the respective introduced changes. c, Augmentation of the ADNI dataset with synthetic data from Cor2Vox, based on in-house cortical shapes from frontotemporal dementia (FTD) cases. A higher multi-reference (MR)-SSIM indicates a more similar image appearance to that of ADNI. Cor2Vox accurately preserved the reduced cortical thickness in the frontotemporal region, a hallmark of FTD [18], compared to ADNI normal controls (CN).

transitioning smoothly between two arbitrary UKB subjects (see also supplementary video). Importantly, the interpolation preserves both gyration and cortical thickness, maintaining characteristic cortical grooves, such as the central sulcus, throughout. In contrast, as shown in Figure 1 and Figure S1, 3D-DDPMs failed to maintain such anatomical realism, often producing non-identifiable and discontinuous gyral patterns that hinder subsequent gyral-based parcellation, such as those based on the Desikan-Killiany (DK) atlas [55]. These parcellations are critical for numerous downstream neuroimaging applications. To assess anatomical plausibility, we applied the DK atlas to randomly generated, interpolation-based synthetic cortical shapes and compared regional cortical thickness against real counterparts. The results, summarized in the scatter plots in Figure 5a and Figure S2, demonstrate that Cor2Vox consistently preserves anatomically realistic cortical thickness across all 34 DK regions.

Next, we compared the geometric consistency between sampled and real cortical shapes with their corresponding reconstructions from the synthesized MRIs. The average symmetric surface distances (ASSD) between sampled cortical surfaces ($n = 323$) and corresponding reconstructions from the synthetic MRIs were 0.246 mm (SD: 0.019 mm) for the left hemisphere and 0.239 mm (SD: 0.016 mm) for the right hemisphere. Conversely, ASSDs for real cortical surfaces from UKB were 0.255 mm (SD: 0.013 mm) and 0.258 mm (SD: 0.012 mm) per hemisphere. These results indicate that new, shape model-derived cortical surfaces integrate seamlessly into Cor2Vox’s image generation process, enabling the realistic synthesis of brains across the broad spectrum of cortical variability.

3.3 Sub-voxel simulation of cortical atrophy

Controlled simulation of sub-voxel cortical atrophy is important for benchmarking methods for cortical surface reconstruction and cortical thickness estimation. To evaluate the sensitivity of Cor2Vox to simulated alterations in cortical morphology, we mimicked progressive cortical thinning ranging from 0.1 to 0.6 mm (image resolution: 1 mm isotropic). As detailed in Section 2.2, atrophy was simulated once globally across the entire cortex and also locally in the temporal lobe. We used the cognitively normal control group from our ADNI test set as a basis for this experiment ($n = 124$). From the synthesized scans, we estimated cortical thickness again with Vox2Cortex-Flow, comparing it to the original (baseline) cortical thickness for each subject.

As shown in Figure 5b, the difference in cortical thickness estimated from the synthetic MRIs closely reflected the magnitude of the imposed changes. Specifically, we obtained a mean absolute error in recovered relative cortical thickness changes of 0.14 mm (SD: 0.08 mm) across all simulations of localized atrophy and, similarly, 0.14 mm (SD: 0.10 mm) for global gray matter atrophy.

3.4 Shape-based image harmonization

Neuroimaging datasets often focus on a single disease, such as Alzheimer’s disease in ADNI. For studying clinically relevant questions, such as the differential diagnosis of dementing disorders, a combination of multiple datasets is needed; yet, this introduces unwanted dataset biases [56]. Cor2Vox addresses this harmonization challenge by generating consistent MRIs from external cortical shapes. Importantly, scans from the target disease do not need to be included in the diffusion model’s training set. We demonstrate this capability by generating MRI scans of patients with frontotemporal dementia (FTD) from cortical shapes obtained from our in-house cohort using the ADNI-trained Cor2Vox.

As shown in Figure 5c, the resulting synthetic scans integrate seamlessly into ADNI, exhibiting significantly higher mean Structural Similarity Index Measure (SSIM) to ten randomly chosen (multi-reference) ADNI scans compared to the original in-house scans. Crucially, these synthesized MRIs retained the characteristic pathological features of FTD, exhibiting significantly lower cortical thickness in the frontotemporal region compared to cognitively normal (CN) subjects, thereby mirroring the characteristic morphology of this type of brain disease [18].

3.5 Analysis of shape-conditioning strategies

In this section, we examine the impact of shape conditioning on the geometric consistency in Cor2Vox, focusing on the choice of shape representations in the source shape domain and the auxiliary shape conditions. See Section 2.1 for methodological details.

Table 1: Influence of different source domains (Source) and auxiliary shape conditions (Aux. Condition) provided to Cor2Vox during the Brownian bridge process. We report the mean \pm SD on the ADNI validation set ($n = 169$). Geometric accuracy is measured in terms of average symmetric surface distance (ASSD) in mm. (\mathcal{S}_p : Pial SDF, \mathcal{S}_w : White matter SDF, \mathcal{S}_c : Cortex SDF, \mathcal{S}_d : Joint cortex DF, \mathcal{E} : Edge map, \mathcal{R} : Cortical ribbon mask)

Source	Aux. Condition	ASSD \downarrow			
		Left Hemisphere		Right Hemisphere	
		White	Pial	White	Pial
\mathcal{S}_p	—	0.375 ± 0.066	0.233 ± 0.021	0.386 ± 0.068	0.236 ± 0.022
\mathcal{S}_w	—	0.289 ± 0.066	0.375 ± 0.031	0.303 ± 0.067	0.376 ± 0.034
\mathcal{E}	—	0.351 ± 0.037	0.307 ± 0.023	0.369 ± 0.042	0.307 ± 0.024
\mathcal{R}	—	0.336 ± 0.034	0.279 ± 0.021	0.335 ± 0.037	0.280 ± 0.022
\mathcal{S}_d	—	0.333 ± 0.039	0.250 ± 0.022	0.342 ± 0.040	0.249 ± 0.021
$\mathcal{S}_p \cap \mathcal{S}_w$	—	0.361 ± 0.087	0.365 ± 0.033	0.373 ± 0.088	0.366 ± 0.033
$\mathcal{S}_p \cup \mathcal{S}_w$	—	0.416 ± 0.083	0.242 ± 0.025	0.429 ± 0.087	0.244 ± 0.026
$\mathcal{S}_p \sqcup_{10} \mathcal{S}_w$	—	0.316 ± 0.076	0.261 ± 0.025	0.331 ± 0.082	0.262 ± 0.027
$\mathcal{S}_p \sqcup_{100} \mathcal{S}_w$	—	0.332 ± 0.065	0.256 ± 0.024	0.339 ± 0.072	0.256 ± 0.025
$\mathcal{S}_p, \mathcal{S}_w^*$	—	0.394 ± 0.074	0.535 ± 0.064	0.418 ± 0.079	0.553 ± 0.071
\mathcal{S}_c	—	0.381 ± 0.066	0.245 ± 0.026	0.390 ± 0.070	0.247 ± 0.026
\mathcal{R}	$\mathcal{S}_p, \mathcal{S}_w$	0.293 ± 0.027	0.262 ± 0.018	0.305 ± 0.031	0.261 ± 0.016
\mathcal{R}	$\mathcal{S}_p, \mathcal{S}_w, \mathcal{E}$	0.301 ± 0.038	0.263 ± 0.021	0.305 ± 0.040	0.264 ± 0.022
\mathcal{S}_d	\mathcal{E}	0.338 ± 0.034	0.305 ± 0.022	0.347 ± 0.037	0.310 ± 0.023
\mathcal{S}_d	\mathcal{R}	0.305 ± 0.037	0.268 ± 0.034	0.316 ± 0.040	0.267 ± 0.038
\mathcal{S}_d	$\mathcal{S}_p, \mathcal{S}_w$	0.310 ± 0.058	0.231 ± 0.015	0.326 ± 0.063	0.234 ± 0.015
\mathcal{S}_c	\mathcal{E}	0.326 ± 0.036	0.241 ± 0.021	0.339 ± 0.039	0.243 ± 0.022
\mathcal{S}_c	\mathcal{R}	0.305 ± 0.030	0.261 ± 0.021	0.312 ± 0.033	0.262 ± 0.020
\mathcal{S}_c	$\mathcal{S}_p, \mathcal{S}_w$	0.310 ± 0.060	0.236 ± 0.020	0.321 ± 0.064	0.239 ± 0.022
\mathcal{S}_c	\mathcal{E}, \mathcal{R}	0.289 ± 0.031	0.252 ± 0.016	0.294 ± 0.034	0.254 ± 0.016
\mathcal{S}_c	$\mathcal{S}_p, \mathcal{S}_w, \mathcal{E}$	0.294 ± 0.043	0.236 ± 0.017	0.311 ± 0.047	0.238 ± 0.018
\mathcal{S}_c	$\mathcal{S}_p, \mathcal{S}_w, \mathcal{R}$	0.305 ± 0.036	0.255 ± 0.019	0.308 ± 0.037	0.255 ± 0.019
\mathcal{S}_c	$\mathcal{S}_p, \mathcal{S}_w, \mathcal{E}, \mathcal{R}$	0.282 ± 0.032	0.250 ± 0.017	0.287 ± 0.035	0.250 ± 0.017

* This model requires two parallel Brownian bridge processes.

3.5.1 Analysis of the primary shape condition

As summarized in Table 1, we first assessed each individual shape condition: pial surface signed distance function (SDF) \mathcal{S}_p , white matter surface SDF \mathcal{S}_w , edge map \mathcal{E} , cortical ribbon mask \mathcal{R} , and cortex SDF \mathcal{S}_c , as single-source domains in the Brownian bridge diffusion process. Conditioning solely on the Pial SDF \mathcal{S}_p yielded the best pial surface accuracy (0.233 ± 0.021 mm ASSD for the left hemisphere), and similarly, white matter SDF \mathcal{S}_w yielded the best white matter accuracy (0.289 ± 0.066 mm). However, in both cases, the model performed poorly on the respective other surface, which was not explicitly specified. The cortical ribbon mask (\mathcal{R}) provided high accuracy on the white matter generation while falling short on the pial surface synthesis.

Next, we investigated different strategies for combining the two complementary surface SDFs, pial surface \mathcal{S}_p and white matter surface \mathcal{S}_w . Specifically, we evaluated intersection ($\mathcal{S}_p \cap \mathcal{S}_w$), union ($\mathcal{S}_p \cup \mathcal{S}_w$), soft union ($\mathcal{S}_p \sqcup_k \mathcal{S}_w$, parameterized by a sharpness factor k), and joint distance function (DF) \mathcal{S}_d , which is formed by summing the distance functions of both surfaces. These combination strategies resulted in poorer performance on at least one surface compared to single-surface conditioning, except \mathcal{S}_d and $\mathcal{S}_p \sqcup_{100} \mathcal{S}_w$ reaching on-par performance. Furthermore, two parallel Brownian bridge processes, conditioned on both \mathcal{S}_p and \mathcal{S}_w , resulted in the worst pial surface accuracy (0.535 ± 0.064 mm), indicating that two simultaneous, uncoordinated Brownian bridge processes introduce inaccuracies.

3.5.2 Analysis of auxiliary shape conditions

Finally, we assessed the impact of providing various shape conditions as auxiliary conditions in Cor2Vox. Those auxiliary conditions are provided as concatenated inputs to the generative model to further guide the generation based on the primary condition, cf. Figure 2. Using the cortex SDF (\mathcal{S}_c) as the primary condition, we progressively introduced combinations of auxiliary inputs ($\mathcal{S}_p, \mathcal{S}_w, \mathcal{E}, \mathcal{R}$). Incorporating more shape cues consistently improved geometric accuracy, as reported in Table 1, with the combination of all four conditions ($\mathcal{S}_p, \mathcal{S}_w, \mathcal{E}, \mathcal{R}$) yielding the best overall consistency. In particular, it enhanced white matter accuracy while maintaining comparable pial surface performance, consistently across hemispheres. We also evaluated using either \mathcal{R} or \mathcal{S}_d as the primary condition in combination with auxiliary inputs, both of which outperformed their original scores (without auxiliary conditioning).

In summary, these results confirm the effectiveness of adopting \mathcal{S}_c as the primary condition in Cor2Vox, and they highlight the benefit of incorporating complementary shape information via the proposed auxiliary conditioning.

4 Discussion

Our study revealed flaws in conventional DDPMs [22], arguably the de facto standard architecture for high-dimensional image generation, when applied to unconditional 3D brain image generation, cf. Section 3.2. Specifically, we found that 3D-DDPMs do not preserve characteristic grooves in the cerebral cortex, such as the central and superior temporal sulci. These irregularities break standardized atlas-based brain parcellation, which is crucial for many downstream neuroscience applications [57]. Our findings align with prior work advocating for rigorous evaluation of synthetic brain MRIs [53], extending these efforts beyond volume-based metrics such as Cohen’s d to include advanced cortical surface reconstruction. In Cor2Vox, we addressed these issues by incorporating an explicit shape model of the cerebral cortex. This guarantees anatomical plausibility and, hence, compatibility with surface-based analysis pipelines and standardized parcellation schemes.

When it comes to brain morphology in synthetic MRIs, conditioning on low-dimensional demographic and clinical covariates, such as age, sex, and diagnosis, is a popular approach [6, 5]. However, the generative capacity of these methods remains, by design, limited to implicit associations between the covariates and structural observations that were included in the training. In addition, such models are prone to inheriting existing biases as their outputs reflect statistical correlations in the training data [8]. In contrast, Cor2Vox readily decouples from the training data, as evidenced by its ability to synthesize images for frontotemporal dementia, a condition not contained in the ADNI training set. Moreover, our results on cortical atrophy simulation showed that Cor2Vox accurately reflected simulated changes imposed on cortical surfaces, cf. Section 3.3. This capability allows researchers to systematically generate edge cases, explore hypothetical or extreme conditions, and stress-test models under controlled variations, an opportunity usually not provided by existing conditional generative models. The reported mean absolute error between introduced and recovered cortical thickness changes of 0.14 mm is in the range of the expected variability of morphometric neuroimaging pipelines for cortical thickness estimation [58, 29].

The capability of capturing continuous simulations also distinguishes Cor2Vox from existing shape-based generative models, such as Pix2Pix [45], BBDM [21], and Med-DDPM [46]. Nevertheless, these approaches represent important baselines for our approach. In our experiments, Cor2Vox outperformed all of them significantly in terms of geometric consistency with the cortical shape priors at comparable image fidelity metrics, cf. Section 3.1. Our ablation study suggests that the combination of the cortex SDF-based Brownian bridge process together with the auxiliary cortex representations (pial SDF, white matter SDF, cortex edge map, and cortical ribbon mask) is the key driver for the high accuracy in Cor2Vox, cf. Section 3.5. Importantly, all of our generated images passed the recommended quality threshold of SynthSeg+ [47], cf. Figure 3, indicating that the synthesized images meet established standards for segmentation reliability, in all structures, not only in cortical gray matter, and are suitable for downstream neuroimaging analyses.

While our framework demonstrated strong performance in generating anatomically realistic brain MRIs conditioned on complex cortical surfaces, it is currently limited to this imaging modality. Specifically, we have not yet explored conditioning on additional anatomical or pathological structures beyond the cerebral cortex, such as subcortical regions or tumors. Nonetheless, we believe the modularity of our framework lends itself well to extension, and conditioning on simpler shapes, such as those found in subcortical structures or lesion masks, should be feasible with dedicated architectural changes. Future work will investigate these directions to broaden the applicability of shape-grounded generative modeling.

5 Conclusion

In summary, Cor2Vox advanced 3D medical image generation through surface-based modeling of anatomical shape. By incorporating a population-scale, mesh-based shape model, Cor2Vox enabled anatomically faithful synthesis of 3D brain MRIs with high geometric fidelity using fine-grained cortical surfaces as structural priors. Our experiments showed strict consistency between the synthesized images and the conditional inputs, demonstrating the capability to perform sub-voxel simulations of cortical atrophy and effectively disentangle brain shape and appearance. Cor2Vox’s ability to produce a variety of phenotypes via anatomically grounded sampling and simula-

tion, without retraining, highlighted its potential as a powerful tool for data augmentation, disease progression modeling, and cross-site harmonization in neuroimaging studies. Together, these results demonstrated that explicit surface-based shape modeling provides a principled and effective foundation for controllable, biologically plausible 3D medical image generation, thereby addressing key limitations in previous generative models.

Data availability

Data from ADNI are available from the LONI website at <https://ida.loni.usc.edu> upon registration and compliance with the data usage agreement. UK Biobank (UKB) data can be requested via the UKB website (<https://www.ukbiobank.ac.uk/>) following their application process. The in-house dataset can be shared upon request. We used the Montreal Neuroimaging Institute MNI152 template for image processing purposes; it is available for download at <http://www.bic.mni.mcgill.ca/ServicesAtlases/ICBM152NLin2009>.

Code availability

Our code is available on GitHub (<https://github.com/ai-med/Cor2Vox>).

Acknowledgments

Y.L. was supported by the Munich Center for Machine Learning (MCML). C.W. received funding from the German Research Foundation (DFG) and the DAAD programme Konrad Zuse Schools of Excellence in Artificial Intelligence, sponsored by the Federal Ministry of Research, Technology, and Space.

Data collection and sharing for this project was funded by the Alzheimer’s Disease Neuroimaging Initiative (ADNI) (National Institutes of Health Grant U01 AG024904) and DOD ADNI (Department of Defense award number W81XWH-12-2-0012). ADNI is funded by the National Institute on Aging, the National Institute of Biomedical Imaging and Bioengineering, and through generous contributions from the following: Alzheimer’s Association; Alzheimer’s Drug Discovery Foundation; Araclon Biotech; BioClinica, Inc.;

Biogen Idec Inc.; BristolMyers Squibb Company; Eisai Inc.; Elan Pharmaceuticals, Inc.; Eli Lilly and Company; EuroImmun; F. Hoffmann-La Roche Ltd and its affiliated company Genentech, Inc.; Fujirebio; GE Healthcare; ; IXICO Ltd.; Janssen Alzheimer Immunotherapy Research & Development, LLC.; Johnson & Johnson Pharmaceutical Research & Development LLC.; Medpace, Inc.; Merck & Co., Inc.; Meso Scale Diagnostics, LLC.; NeuroRx Research; Neurotrack Technologies; Novartis Pharmaceuticals Corporation; Pfizer Inc.; Piramal Imaging; Servier; Synarc Inc.; and Takeda Pharmaceutical Company. The Canadian Institutes of Health Research is providing funds to support ADNI clinical sites in Canada. Private sector contributions are facilitated by the Foundation for the National Institutes of Health (www.fnih.org). The grantee organization is the Northern California Institute for Research and Education, and the study is coordinated by the Alzheimer's Disease Cooperative Study at the University of California, San Diego. ADNI data are disseminated by the Laboratory for Neuro Imaging at the University of Southern California.

Data used in the preparation of this article were obtained from the UK Biobank Resource under Application No. 34479.

We thank Dr. med. Dennis Hedderich for providing clinical MRI scans from 10 patients, which supported the evaluation of Cor2Vox on frontotemporal dementia.

We further gratefully acknowledge the scientific support and resources of the AI service infrastructure LRZ AI Systems provided by the Leibniz Supercomputing Centre (LRZ).

References

- [1] Boris van Breugel, Tennison Liu, Dino Oglic, and Mihaela van der Schaar. Synthetic data in biomedicine via generative artificial intelligence. *Nature Reviews Bioengineering*, 2(12):991–1004, October 2024.
- [2] Li Sun, Junxiang Chen, Yanwu Xu, Mingming Gong, Ke Yu, and Kayhan Batmanghelich. Hierarchical amortized gan for 3d high resolution medical image synthesis. *IEEE Journal of Biomedical and Health Informatics*, 26(8):3966–3975, 2022.
- [3] Firas Khader, Gustav Müller-Franzes, Soroosh Tayebi Arasteh, Tianyu Han, Christoph Haarburger, Maximilian Schulze-Hagen, Philipp Schad, Sandy Engelhardt, Bettina Baeßler, Sebastian Foersch, Johannes Stegmaier, Christiane Kuhl, Sven Nebelung, Jakob Nikolas Kather, and Daniel Truhn. Denoising diffusion probabilistic models for 3d medical image generation. *Scientific Reports*, 13(1), May 2023.
- [4] Bardia Khosravi, Frank Li, Theo Dapamede, Pouria Rouzrokh, Cooper U. Gamble, Hari M. Trivedi, Cody C. Wyles, Andrew B. Seller-gren, Saptarshi Purkayastha, Bradley J. Erickson, and Judy W. Gichoya. Synthetically enhanced: unveiling synthetic data’s potential in medical imaging research. *eBioMedicine*, 104:105174, June 2024.
- [5] Petru-Daniel Tudosiu, Walter H. L. Pinaya, Pedro Ferreira Da Costa, Jessica Dafflon, Ashay Patel, Pedro Borges, Virginia Fernandez, Mark S. Graham, Robert J. Gray, Parashkev Nachev, Sebastien Ourselin, and M. Jorge Cardoso. Realistic morphology-preserving generative modelling of the brain. *Nature Machine Intelligence*, 6(7):811–819, 2024.
- [6] Wei Peng, Tomas Bosschieter, Jiahong Ouyang, Robert Paul, Edith V. Sullivan, Adolf Pfefferbaum, Ehsan Adeli, Qingyu Zhao, and Kilian M. Pohl. Metadata-conditioned generative models to synthesize anatomically-plausible 3d brain MRIs. *Medical Image Analysis*, 98:103325, 2024.
- [7] Jinzhuo Wang, Kai Wang, Yunfang Yu, Yuxing Lu, Wenchao Xiao, Zhuo Sun, Fei Liu, Zixing Zou, Yuanxu Gao, Lei Yang, Hong-Yu Zhou, Hanpei Miao, Wenting Zhao, Lisha Huang, Lingchao Zeng, Rui Guo, Ieng

Chong, Boyu Deng, Linling Cheng, Xiaoniao Chen, Jing Luo, Meng-Hua Zhu, Daniel Baptista-Hon, Olivia Monteiro, Ming Li, Yu Ke, Jiahui Li, Simiao Zeng, Taihua Guan, Jin Zeng, Kanmin Xue, Eric Oermann, Huiyan Luo, Yun Yin, Kang Zhang, and Jia Qu. Self-improving generative foundation model for synthetic medical image generation and clinical applications. *Nature Medicine*, 31(2):609–617, 2024.

- [8] Burak Koçak, Andrea Ponsiglione, Arnaldo Stanzione, Christian Bluethgen, João Santinha, Lorenzo Ugga, Merel Huisman, Michail E. Klontzas, Roberto Cannella, and Renato Cuocolo. Bias in artificial intelligence for medical imaging: fundamentals, detection, avoidance, mitigation, challenges, ethics, and prospects. *Diagnostic and Interventional Radiology*, July 2024.
- [9] Salman Ul Hassan Dar, Marvin Seyfarth, Isabelle Ayx, Theano Papavassiliu, Stefan O. Schoenberg, Robert Malte Siepmann, Fabian Christopher Laqua, Jannik Kahmann, Norbert Frey, Bettina Baeßler, Sebastian Foersch, Daniel Truhn, Jakob Nikolas Kather, and Sandy Engelhardt. Unconditional latent diffusion models memorize patient imaging data. *Nature Biomedical Engineering*, 2025.
- [10] Ilia Shumailov, Zakhar Shumaylov, Yiren Zhao, Nicolas Papernot, Ross Anderson, and Yarin Gal. AI models collapse when trained on recursively generated data. *Nature*, 631(8022):755–759, July 2024.
- [11] Matthew Tivnan, Siyeop Yoon, Zhennong Chen, Xiang Li, Dufan Wu, and Quanzheng Li. Hallucination index: An image quality metric for generative reconstruction models. In *Medical Image Computing and Computer Assisted Intervention – MICCAI 2024*, page 449–458. Springer Nature Switzerland, 2024.
- [12] Keyu Guo, Yongle Huang, Tinglei Jia, Xiangyu Song, Shijie Sun, Hongkai Wei, Xian-Feng Han, Shuwen Huang, Nicola Strisciuglio, and Shuyan Li. Visual grounding in 2d and 3d: A unified perspective and survey. *Information Fusion*, 126:103625, February 2026.
- [13] Lvmin Zhang, Anyi Rao, and Maneesh Agrawala. Adding conditional control to text-to-image diffusion models. In *Proceedings of the IEEE/CVF International Conference on Computer Vision (ICCV)*, pages 3836–3847, 2023.

[14] Pengfei Guo, Can Zhao, Dong Yang, Ziyue Xu, Vishwesh Nath, Yucheng Tang, Benjamin Simon, Mason Belue, Stephanie Harmon, Baris Turkbey, and Daguang Xu. MAISI: Medical AI for synthetic imaging. In *2025 IEEE/CVF Winter Conference on Applications of Computer Vision (WACV)*, page 4430–4441. IEEE, 2025.

[15] Yash Deo, Haoran Dou, Nishant Ravikumar, Alejandro F. Frangi, and Toni Lassila. Shape-guided conditional latent diffusion models for synthesising brain vasculature. In *Deep Generative Models*, page 164–173. Springer Nature Switzerland, 2024.

[16] Diederik P. Kingma and Max Welling. Auto-encoding variational Bayes. In *2nd International Conference on Learning Representations, ICLR 2014, Banff, AB, Canada, April 14-16, 2014, Conference Track Proceedings*, 2014.

[17] R. A. I. Bethlehem, J. Seidlitz, S. R. White, J. W. Vogel, K. M. Anderson, C. Adamson, S. Adler, G. S. Alexopoulos, E. Anagnosoustou, A. Areces-Gonzalez, D. E. Astle, B. Auyeung, M. Ayub, J. Bae, G. Ball, S. Baron-Cohen, R. Beare, S. A. Bedford, V. Benegal, F. Beyer, J. Blangero, M. Blesa Cábez, J. P. Boardman, M. Borzage, J. F. Bosch-Bayard, N. Bourke, V. D. Calhoun, M. M. Chakravarty, C. Chen, C. Chertavian, G. Chetelat, Y. S. Chong, J. H. Cole, A. Corvin, M. Costantino, E. Courchesne, F. Crivello, V. L. Cropley, J. Crosbie, N. Crossley, M. Delarue, R. Delorme, S. Desrivieres, G. A. Devenyi, M. A. Di Biase, R. Dolan, K. A. Donald, G. Donohoe, K. Dunlop, A. D. Edwards, J. T. Elison, C. T. Ellis, J. A. Elman, L. Eyler, D. A. Fair, E. Feczko, P. C. Fletcher, P. Fonagy, C. E. Franz, L. Galan-Garcia, A. Gholipour, J. Giedd, J. H. Gilmore, D. C. Glahn, I. M. Goodyer, P. E. Grant, N. A. Groenewold, F. M. Gunning, R. E. Gur, R. C. Gur, C. F. Hammill, O. Hansson, T. Hedden, A. Heinz, R. N. Henson, K. Heuer, J. Hoare, B. Holla, A. J. Holmes, R. Holt, H. Huang, K. Im, J. Ipser, C. R. Jack, A. P. Jackowski, T. Jia, K. A. Johnson, P. B. Jones, D. T. Jones, R. S. Kahn, H. Karlsson, L. Karlsson, R. Kawashima, E. A. Kelley, S. Kern, K. W. Kim, M. G. Kitzbichler, W. S. Kremen, F. Lalonde, B. Landeau, S. Lee, J. Lerch, J. D. Lewis, J. Li, W. Liao, C. Liston, M. V. Lombardo, J. Lv, C. Lynch, T. T. Mallard, M. Marcelis, R. D. Markello, S. R. Mathias, B. Mazoyer, P. McGuire, M. J. Meaney, A. Mechelli, N. Medic, B. Misic, S. E. Morgan, D. Mothersill, J. Nigg,

M. Q. W. Ong, C. Ortinau, R. Ossenkoppele, M. Ouyang, L. Palaniyappan, L. Paly, P. M. Pan, C. Pantelis, M. M. Park, T. Paus, Z. Pausova, D. Paz-Linares, A. Pichet Binette, K. Pierce, X. Qian, J. Qiu, A. Qiu, A. Raznahan, T. Rittman, A. Rodrigue, C. K. Rollins, R. Romero-Garcia, L. Ronan, M. D. Rosenberg, D. H. Rowitch, G. A. Salum, T. D. Satterthwaite, H. L. Schaare, R. J. Schachar, A. P. Schultz, G. Schumann, M. Schöll, D. Sharp, R. T. Shinozaki, I. Skoog, C. D. Smyser, R. A. Sperling, D. J. Stein, A. Stoliczyn, J. Suckling, G. Sullivan, Y. Taki, B. Thyreau, R. Toro, N. Traut, K. A. Tsvetanov, N. B. Turk-Browne, J. J. Tuulari, C. Tzourio, E. Vachon-Presseau, M. J. Valdes-Sosa, P. A. Valdes-Sosa, S. L. Valk, T. van Amelsvoort, S. N. Vandekar, L. Vasung, L. W. Victoria, S. Villeneuve, A. Villringer, P. E. Vértes, K. Wagstyl, Y. S. Wang, S. K. Warfield, V. Warrier, E. Westman, M. L. Westwater, H. C. Whalley, A. V. Witte, N. Yang, B. Yeo, H. Yun, A. Zalesky, H. J. Zar, A. Zettergren, J. H. Zhou, H. Ziauddeen, A. Zugman, X. N. Zuo, C. Rowe, G. B. Frisoni, A. Pichet Binette, E. T. Bullmore, and A. F. Alexander-Bloch. Brain charts for the human lifespan. *Nature*, 604(7906):525–533, 2022.

- [18] A.-T. Du, N. Schuff, J. H. Kramer, H. J. Rosen, M. L. Gorno-Tempini, K. Rankin, B. L. Miller, and M. W. Weiner. Different regional patterns of cortical thinning in Alzheimer’s disease and frontotemporal dementia. *Brain*, 130(4):1159–1166, 2006.
- [19] Bruce Fischl. FreeSurfer. *NeuroImage*, 62(2):774–781, 2012.
- [20] Christian Gaser, Robert Dahnke, Paul M Thompson, Florian Kurth, Eileen Luders, and the Alzheimer’s Disease Neuroimaging Initiative. CAT: a computational anatomy toolbox for the analysis of structural MRI data. *GigaScience*, 13:giae049, 2024.
- [21] Bo Li, Kaitao Xue, Bin Liu, and Yu-Kun Lai. BBDM: Image-to-image translation with Brownian bridge diffusion models. In *Proceedings of the IEEE/CVF Conference on Computer Vision and Pattern Recognition*, pages 1952–1961, 2023.
- [22] Jonathan Ho, Ajay Jain, and Pieter Abbeel. Denoising diffusion probabilistic models. In *Advances in Neural Information Processing Systems*, volume 33, pages 6840–6851. Curran Associates, Inc., 2020.

- [23] Cathie Sudlow, John Gallacher, Naomi Allen, Valerie Beral, Paul Burton, John Danesh, Paul Downey, Paul Elliott, Jane Green, Martin Landray, Bette Liu, Paul Matthews, Giok Ong, Jill Pell, Alan Silman, Alan Young, Tim Sprosen, Tim Peakman, and Rory Collins. UK Biobank: An open access resource for identifying the causes of a wide range of complex diseases of middle and old age. *PLOS Medicine*, 12(3):e1001779, 2015.
- [24] B. Karacali and C. Davatzikos. Simulation of tissue atrophy using a topology preserving transformation model. *IEEE Transactions on Medical Imaging*, 25(5):649–652, 2006.
- [25] S. Sharma, V. Noblet, F. Rousseau, F. Heitz, L. Rumbach, and J.-P. Armstrong. Evaluation of brain atrophy estimation algorithms using simulated ground-truth data. *Medical Image Analysis*, 14(3):373–389, 2010.
- [26] O. Camara, M. Schweiger, R.I. Scahill, W.R. Crum, B.I. Sneller, J.A. Schnabel, G.R. Ridgway, D.M. Cash, D.L.G. Hill, and N.C. Fox. Phenomenological model of diffuse global and regional atrophy using finite-element methods. *IEEE Transactions on Medical Imaging*, 25(11):1417–1430, 2006.
- [27] Andrew D. Castellano Smith, William R. Crum, Derek L. G. Hill, Neil A. Thacker, and Paul A. Bromiley. Biomechanical simulation of atrophy in mr images. In *Medical Imaging 2003: Image Processing*, volume 5032, page 481. SPIE, 2003.
- [28] Bishesh Khanal, Marco Lorenzi, Nicholas Ayache, and Xavier Pennec. A biophysical model of brain deformation to simulate and analyze longitudinal MRIs of patients with Alzheimer’s disease. *NeuroImage*, 134:35–52, 2016.
- [29] Filip Rusak, Rodrigo Santa Cruz, Léo Lebrat, Ondrej Hlinka, Jurgen Fripp, Elliot Smith, Clinton Fookes, Andrew P. Bradley, and Pierrick Bourgeat. Quantifiable brain atrophy synthesis for benchmarking of cortical thickness estimation methods. *Medical Image Analysis*, 82:102576, 2022.

- [30] Fabian Bongratz, Yitong Li, Sama Elbaroudy, and Christian Wachinger. 3d shape-to-image Brownian bridge diffusion for brain MRI synthesis from cortical surfaces. In *Information Processing in Medical Imaging*, page 187–202. Springer Nature Switzerland, 2025.
- [31] Fabian Bongratz, Anne-Marie Rickmann, and Christian Wachinger. Neural deformation fields for template-based reconstruction of cortical surfaces from MRI. *Medical Image Analysis*, 93:103093, 2024.
- [32] Benjamin Billot, Douglas N. Greve, Oula Puonti, Axel Thielscher, Koen Van Leemput, Bruce Fischl, Adrian V. Dalca, and Juan Eugenio Iglesias. Synthseg: Segmentation of brain MRI scans of any contrast and resolution without retraining. *Medical Image Analysis*, 86:102789, 2023.
- [33] Eungbean Lee, Somi Jeong, and Kwanghoon Sohn. Ebdm: Exemplar-guided image translation with Brownian-bridge diffusion models. In *Computer Vision – ECCV 2024*, page 306–323. Springer Nature Switzerland, 2024.
- [34] Jiaming Song, Chenlin Meng, and Stefano Ermon. Denoising diffusion implicit models. In *International Conference on Learning Representations*, 2021.
- [35] Prafulla Dhariwal and Alexander Quinn Nichol. Diffusion models beat GANs on image synthesis. In *Advances in Neural Information Processing Systems*, 2021.
- [36] Diederik P. Kingma and Jimmy Ba. Adam: A method for stochastic optimization. In *ICLR 2015*, 2015.
- [37] Riddhish Bhalodia, Shireen Elhabian, Jadie Adams, Wenzheng Tao, Ladislav Kavan, and Ross Whitaker. DeepSSM: A blueprint for image-to-shape deep learning models. *Medical Image Analysis*, 91:103034, 2024.
- [38] Jadie Adams, Nawazish Khan, Alan Morris, and Shireen Elhabian. Spatiotemporal cardiac statistical shape modeling: A data-driven approach. In *Statistical Atlases and Computational Models of the Heart. Regular and CMRxMotion Challenge Papers*, page 143–156. Springer Nature Switzerland, 2022.

- [39] Lennart Bastian, Alexander Baumann, Emily Hoppe, Vincent Bürgin, Ha Young Kim, Mahdi Saleh, Benjamin Busam, and Nassir Navab. S3M: Scalable statistical shape modeling through unsupervised correspondences. In *Medical Image Computing and Computer Assisted Intervention – MICCAI 2023*, page 459–469. Springer Nature Switzerland, 2023.
- [40] Bruce Fischl, Martin I. Sereno, Roger B.H. Tootell, and Anders M. Dale. High-resolution intersubject averaging and a coordinate system for the cortical surface. *Human Brain Mapping*, 8(4):272–284, 1999.
- [41] Ken Shoemake. Animating rotation with quaternion curves. In *Proceedings of the 12th annual conference on computer graphics and interactive techniques*, pages 245–254, 1985.
- [42] Marnie E. Shaw, Perminder S. Sachdev, Kaarin J. Anstey, and Nicolas Cherbuin. Age-related cortical thinning in cognitively healthy individuals in their 60s: the path through life study. *Neurobiology of Aging*, 39:202–209, 2016.
- [43] Gina R. Kuperberg, Matthew R. Broome, Philip K. McGuire, Anthony S. David, Marianna Eddy, Fujiro Ozawa, Donald Goff, W. Caroline West, Steven C. R. Williams, Andre J. W. van der Kouwe, David H. Salat, Anders M. Dale, and Bruce Fischl. Regionally localized thinning of the cerebral cortex in schizophrenia. *Archives of General Psychiatry*, 60(9):878, 2003.
- [44] V. Singh, H. Chertkow, J. P. Lerch, A. C. Evans, A. E. Dorr, and N. J. Kabani. Spatial patterns of cortical thinning in mild cognitive impairment and Alzheimer’s disease. *Brain*, 129(11):2885–2893, 2006.
- [45] Phillip Isola, Jun-Yan Zhu, Tinghui Zhou, and Alexei A. Efros. Image-to-image translation with conditional adversarial networks. In *2017 IEEE Conference on Computer Vision and Pattern Recognition (CVPR)*, page 5967–5976. IEEE, 2017.
- [46] Zolnamar Dorjsembe, Hsing-Kuo Pao, Sodtavilan Odonchimed, and Furen Xiao. Conditional diffusion models for semantic 3d brain MRI synthesis. *IEEE Journal of Biomedical and Health Informatics*, 28(7):4084–4093, 2024.

- [47] Benjamin Billot, Colin Magdamo, You Cheng, Steven E. Arnold, Sudeshna Das, and Juan Eugenio Iglesias. Robust machine learning segmentation for large-scale analysis of heterogeneous clinical brain MRI datasets. *Proceedings of the National Academy of Sciences*, 120(9):e2216399120, 2023.
- [48] R. C. Petersen, P. S. Aisen, L. A. Beckett, M. C. Donohue, A. C. Gamst, D. J. Harvey, C. R. Jack, W. J. Jagust, L. M. Shaw, A. W. Toga, J. Q. Trojanowski, and M. W. Weiner. Alzheimer’s disease neuroimaging initiative (ADNI): Clinical characterization. *Neurology*, 74(3):201–209, 2010.
- [49] Thomas J. Littlejohns, Jo Holliday, Lorna M. Gibson, Steve Garratt, Niels Oesingmann, Fidel Alfaro-Almagro, Jimmy D. Bell, Chris Boultwood, Rory Collins, Megan C. Conroy, Nicola Crabtree, Nicola Doherty, Alejandro F. Frangi, Nicholas C. Harvey, Paul Leeson, Karla L. Miller, Stefan Neubauer, Steffen E. Petersen, Jonathan Sellors, Simon Sheard, Stephen M. Smith, Cathie L. M. Sudlow, Paul M. Matthews, and Naomi E. Allen. The UK Biobank imaging enhancement of 100,000 participants: rationale, data collection, management and future directions. *Nature communications*, 11(1):2624, 2020.
- [50] Songrit Maneewongvatana and David Mount. Analysis of approximate nearest neighbor searching with clustered point sets. In *Data Structures, Near Neighbor Searches, and Methodology: Fifth and Sixth DIMACS Implementation Challenges*, page 105–123. American Mathematical Society, 2002.
- [51] Andrew Hoopes, Jocelyn S. Mora, Adrian V. Dalca, Bruce Fischl, and Malte Hoffmann. SynthStrip: skull-stripping for any brain image. *NeuroImage*, 260:119474, 2022.
- [52] Ian Goodfellow, Jean Pouget-Abadie, Mehdi Mirza, Bing Xu, David Warde-Farley, Sherjil Ozair, Aaron Courville, and Yoshua Bengio. Generative adversarial nets. In *Advances in Neural Information Processing Systems*, volume 27. Curran Associates, Inc., 2014.
- [53] Jiaqi Wu, Wei Peng, Binxu Li, Yu Zhang, and Kilian M. Pohl. Evaluating the quality of brain MRI generators. In *Medical Image Computing*

and Computer Assisted Intervention – MICCAI 2024, page 297–307. Springer Nature Switzerland, 2024.

- [54] Bahram Jafrasteh, Wei Peng, Cheng Wan, Yimin Luo, Ehsan Adeli, and Qingyu Zhao. WASABI: A metric for evaluating morphometric plausibility of synthetic brain MRIs, 2025.
- [55] Rahul S. Desikan, Florent Ségonne, Bruce Fischl, Brian T. Quinn, Bradford C. Dickerson, Deborah Blacker, Randy L. Buckner, Anders M. Dale, R. Paul Maguire, Bradley T. Hyman, Marilyn S. Albert, and Ronald J. Killiany. An automated labeling system for subdividing the human cerebral cortex on MRI scans into gyral based regions of interest. *NeuroImage*, 31(3):968–980, 2006.
- [56] Christian Wachinger, Anna Rieckmann, and Sebastian Pölsterl. Detect and correct bias in multi-site neuroimaging datasets. *Medical Image Analysis*, 67:101879, 2021.
- [57] Ross M. Lawrence, Eric W. Bridgeford, Patrick E. Myers, Ganesh C. Arvapalli, Sandhya C. Ramachandran, Derek A. Pisner, Paige F. Frank, Allison D. Lemmer, Aki Nikolaidis, and Joshua T. Vogelstein. Standardizing human brain parcellations. *Scientific Data*, 8(1), March 2021.
- [58] Xiao Han, Jorge Jovicich, David Salat, Andre van der Kouwe, Brian Quinn, Sylvester Czanner, Evelina Busa, Jenni Pacheco, Marilyn Albert, Ronald Killiany, Paul Maguire, Diana Rosas, Nikos Makris, Anders Dale, Bradford Dickerson, and Bruce Fischl. Reliability of MRI-derived measurements of human cerebral cortical thickness: The effects of field strength, scanner upgrade and manufacturer. *NeuroImage*, 32(1):180–194, August 2006.

Supplementary Material



Figure S1: Reconstructed cortical surfaces of the right hemisphere from 20 arbitrarily sampled brain MRIs using 3D-DDPM. They suffer from flaws in anatomical plausibility, such as irregular, discontinuous grooves and misplaced folds.

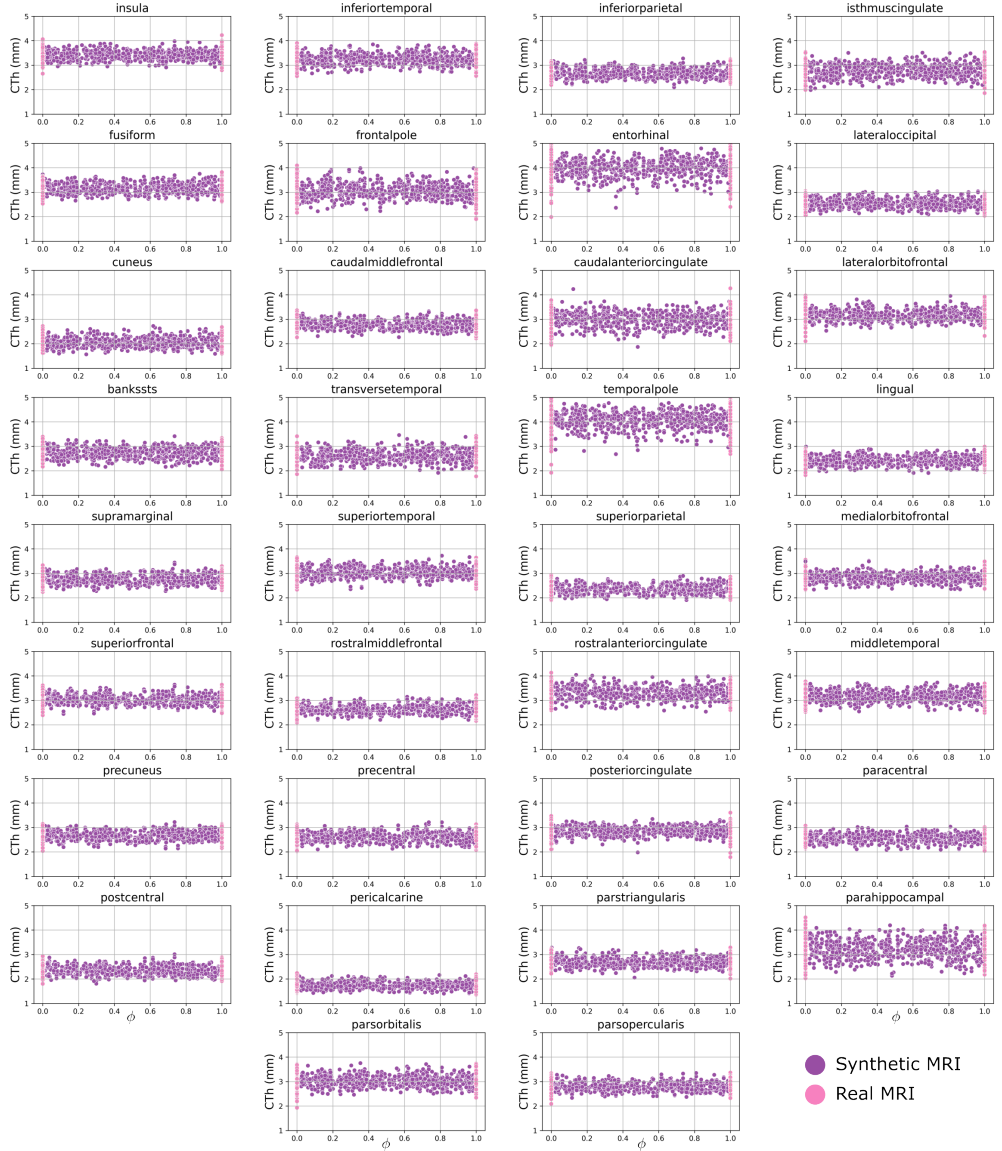


Figure S2: Comparison of regional cortical thickness (CTh) in real and synthetic MRIs by Cor2Vox based on the Desikan-Killany atlas. Cor2Vox preserves the magnitude and spread of cortical thickness observed in real-world data across all 34 DK regions.

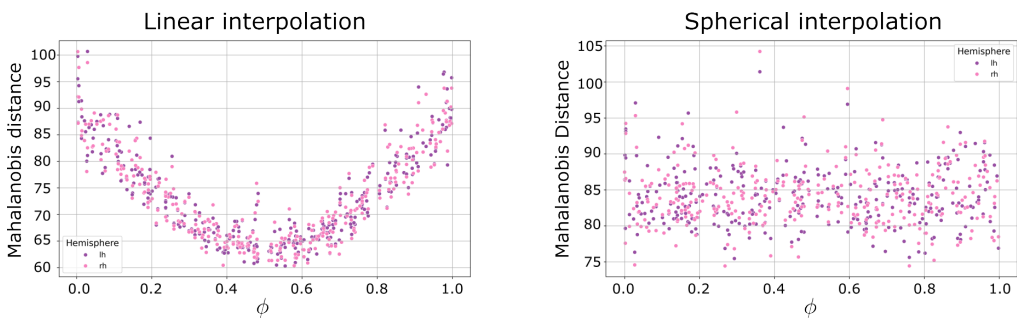


Figure S3: Mahalanobis distance of cortical shapes to the population mean in PCA latent space for linear (left) and spherical (right) interpolation. $0 < \phi < 1$ denotes the interpolation factor, with $\phi = 0/1$ corresponding to real samples. While linear interpolation tends to drift toward the mean, yielding implausibly smooth shapes, spherical interpolation circumvents this issue, producing more realistic cortex shapes.

Table S1: Image fidelity comparison of implemented methods for 3D brain MRI generation. Structural similarity index measure (SSIM↑) and peak signal-to-noise ratio (PSNR↑) quantify whole-brain image fidelity, and average symmetric surface distance (ASSD↓, mm) measures geometric consistency of white matter (WM) and pial cortical surfaces. Values represent the mean and standard deviation across all samples in our test set ($n = 323$).

Model	ASSD↓					
	Whole Brain		Left Hemisphere		Right Hemisphere	
	SSIM↑	PSNR↑	WM	Pial	WM	Pial
Pix2Pix $_{\mathcal{E}}$ [45] [*]	$0.891_{\pm 0.011}$	$24.76_{\pm 1.96}$	$0.784_{\pm 0.190}$	$0.853_{\pm 0.227}$	$0.760_{\pm 0.174}$	$0.804_{\pm 0.195}$
Med-DDPM $_{\mathcal{E}}$ [46]	$0.894_{\pm 0.015}$	$22.38_{\pm 2.63}$	$0.506_{\pm 0.042}$	$0.437_{\pm 0.027}$	$0.516_{\pm 0.043}$	$0.436_{\pm 0.026}$
BBDM $_{\mathcal{E}}$ [21] [*]	$0.898_{\pm 0.020}$	$19.95_{\pm 2.61}$	$0.349_{\pm 0.032}$	$0.307_{\pm 0.021}$	$0.368_{\pm 0.035}$	$0.307_{\pm 0.021}$
Pix2Pix $_{\mathcal{R}}$ [45] [*]	$0.885_{\pm 0.013}$	$23.69_{\pm 2.06}$	$0.697_{\pm 0.137}$	$0.691_{\pm 0.155}$	$0.698_{\pm 0.183}$	$0.680_{\pm 0.221}$
Med-DDPM $_{\mathcal{R}}$ [46]	$0.899_{\pm 0.016}$	$22.30_{\pm 2.80}$	$0.359_{\pm 0.043}$	$0.347_{\pm 0.034}$	$0.373_{\pm 0.106}$	$0.352_{\pm 0.101}$
BBDM $_{\mathcal{R}}$ [21] [*]	$0.898_{\pm 0.021}$	$19.67_{\pm 2.54}$	$0.328_{\pm 0.037}$	$0.283_{\pm 0.034}$	$0.338_{\pm 0.128}$	$0.287_{\pm 0.121}$
Cor2Vox/DDPM	$0.902_{\pm 0.015}$	$23.13_{\pm 2.71}$	$0.335_{\pm 0.038}$	$0.300_{\pm 0.033}$	$0.348_{\pm 0.048}$	$0.305_{\pm 0.037}$
Cor2Vox	$0.906_{\pm 0.018}$	$21.10_{\pm 2.74}$	$0.283_{\pm 0.029}$	$0.251_{\pm 0.019}$	$0.289_{\pm 0.031}$	$0.251_{\pm 0.017}$

^{*} Method adapted for 3D image generation.

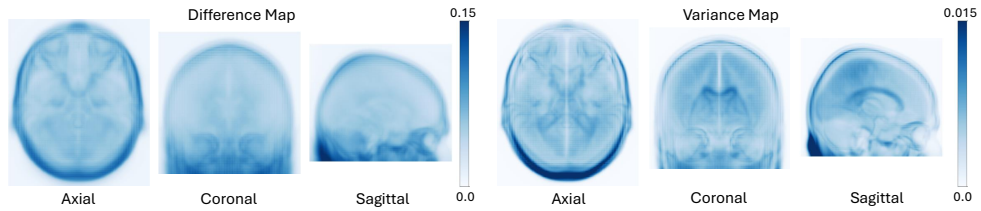


Figure S4: Generation variability in Cor2Vox outputs. We present the mean absolute voxel-wise difference between synthetic MRIs generated from Cor2Vox and corresponding original MRIs (with the same cortical shape), as well as voxel-wise variance in synthetic MRIs across five random seeds, based on the ADNI test set ($n = 323$). Values are averaged along the three anatomical axes. Darker colors indicate higher difference/variability.

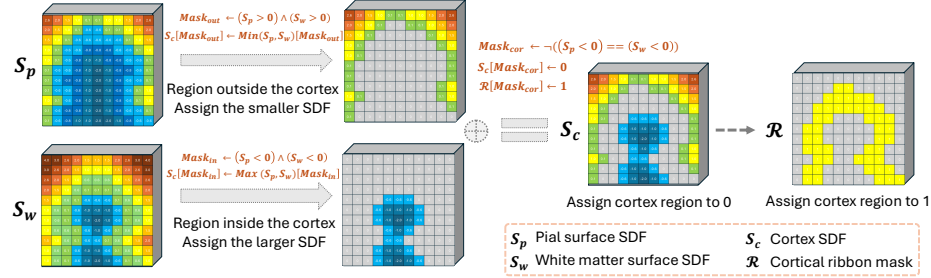


Figure S5: Generation of cortex SDF (S_c) and cortical ribbon mask (\mathcal{R}).